LAWRENCE
LIVERMORE
NATIONAL
LABORATORY

LLNL-JRNL-404406

A Refractory Inclusion Returned by Stardust from Comet 81P/Wild 2

S. B. Simon, D. J. Joswiak, H. A. Ishii, J. P. Bradley, M. Chi, L. Grossman, J. Aléon, D. E. Brownlee, S. Fallon, I. D. Hutcheon, G. Matrajt, K. D. McKeegan

June 3, 2008

Meteoritics and Planetary Science

Disclaimer

A Refractory Inclusion Returned by Stardust from Comet 81P/Wild 2

S. B. Simon[1*], D. J. Joswiak[2], H. A. Ishii[3], J. P. Bradley[3], M. Chi[3,4], L. Grossman[1,5], J. Aléon[6,7], D. E. Brownlee[2], S. Fallon[3,8], I. D. Hutcheon[3,6], G. Matrajt[2], and K. D. McKeegan[9]

[1]Department of the Geophysical Sciences, The University of Chicago, 5734 S. Ellis Ave., Chicago, IL 60637 USA

[2]Department of Astronomy, University of Washington, Seattle, WA 98195 USA

[3]Institute for Geophysics and Planetary Physics, Lawrence Livermore National Laboratory, 7000 East Avenue, Livermore, CA 94550 USA

[4]Department of Chemical Engineering and Materials Science, University of California Davis, 1 Shields Ave., Davis, CA 95616 USA

[5]Enrico Fermi Institute, The University of Chicago, 5640 S. Ellis Ave., Chicago, IL 60637 USA

[6]Glenn T. Seaborg Institute, Lawrence Livermore National Laboratory, P.O. Box 808, Livermore, CA 94551 USA

[7]Centre de Spectrométrie Nucléaire et de Spectrométrie de Masse, Bât 104, 91405 Orsay campus, France

[8]SSAMS Radiocarbon Dating Laboratory, RSES, The Australian National University, Canberra, ACT 0200 Australia

[9]Department of Earth and Space Sciences, University of California Los Angeles, Los Angeles, CA 90095 USA

Submitted to *Meteoritics & Planetary Science*
December 19, 2007
Revised May 2008

*Correspondence author: sbs8@uchicago.edu

ABSTRACT

Among the samples returned from comet 81P/Wild 2 by the Stardust spacecraft is a suite of particles from one impact track (Track 25) that are Ca-, Al-rich and FeO-free. We studied three particles from this track that range in size from 5.3 × 3.2 μm to 15 × 10 μm. Scanning and transmission electron microscopy show that they consist of very fine-grained (from ~0.5 to ~2 μm) Al-rich, Ti-bearing and Ti-free clinopyroxene, Mg-Al spinel, anorthite, perovskite, and osbornite (TiN). In addition to these phases, the terminal particle, named "Inti", also contains melilite. All of these phases, with the exception of osbornite, are common in refractory inclusions and are predicted to condense at high temperature from a gas of solar composition. Osbornite, though very rare, has also been found in meteoritic refractory inclusions, and could have formed in a region of the nebula where carbon became enriched relative to oxygen compared to solar composition. Compositions of Ti-pyroxene in Inti are similar, but not identical, to those of fassaite from Allende inclusions. Electron energy loss spectroscopy shows that Ti-rich pyroxene in Inti has Ti^{3+}/Ti^{4+} within the range of typical meteoritic fassaite, consistent with formation under reducing conditions comparable to those of a system of solar composition. Inti is ^{16}O-rich, with $\delta^{18}O \approx \delta^{17}O \approx -40‰$, like unaltered phases in refractory inclusions and refractory IDPs. With grain sizes, mineralogy, mineral chemistry, and an oxygen isotopic composition like those of refractory inclusions, we conclude that Inti is a refractory inclusion that formed in the inner solar nebula. Identification of a particle that formed in the inner Solar System among the comet samples demonstrates that there was transport of materials from the inner to the outer nebula, probably either in a bipolar outflow or by turbulence.

INTRODUCTION

The primary goal of the Stardust comet sample return mission was to do laboratory studies on materials found in a Jupiter-family comet which, like all similar comets, is believed to have formed at the edge of the solar nebula disk, just beyond the orbit of Neptune. The comet samples are likely to be a representative sampling of the non-volatile particulate matter that was

at the outer edge of the Solar System at the time of its origin. An additional goal of returning samples from a comet was to see which, if any, of the extraterrestrial samples in our collections could have come from comets. It has long been understood that cometary particles must be present among our collections of interplanetary dust particles (IDPs) (Bradley and Brownlee 1986; Brownlee et al. 1995; Rietmeijer 1998), but without documented comet samples for comparison it has been impossible to confirm which IDPs are, in fact, from comets. In addition, it is possible that comet nuclei have features in common with carbonaceous chondrite meteorites (McSween and Weissman 1989; Gounelle et al. 2006). By making a connection between materials from comet 81P/Wild 2 returned by the Stardust mission and well-characterized IDPs and/or meteoritic samples, we can improve our understanding of these primitive samples, and especially of cometary matter. Analytical results for a comet sample that represents a link between meteorites and 81P/Wild 2 are reported in this paper.

As described in detail elsewhere (e.g., Brownlee et al. 2006), samples from the nucleus of 81P/Wild 2 were collected in aerogel that was exposed during a flyby on January 2, 2004 and delivered to Earth by the Stardust spacecraft on January 15, 2006. Aerogel is a porous glass typically composed of interconnected nanometer-sized silica clusters. The Stardust aerogel has a bulk density <0.05 g-cm^{-3} and was designed to minimize modification of grains during their capture. Numerous micron- to > ~10 μm-scale cometary particles were collected, and they experienced a wide range of degrees of melting and fragmentation during capture by deceleration in the aerogel, but most components larger than 1 μm were captured intact without significant alteration (Zolensky et al. 2006). This process resulted in the formation of visible tracks in the aerogel. A typical track has fine debris ±visible particles along its surface and one or more "terminal particles" at the end furthest from the original exposed aerogel surface. Tracks were assigned numbers, and all material from a given track is identified with that number. The specific samples that are the subject of this paper are the terminal particle and two sub-terminal particles from Track 25 (C2054, 4, 25). A plan view optical micrograph of this track, after removal of the terminal particle but prior to sampling of the sub-terminal particles, is shown in Fig. 1. The terminal particle was named "Inti", after the Incan sun god, and the sub-terminal particles we studied are Inti-B and Inti-C (Fig. 1). Other particles can be seen in Fig. 1, but these have not yet been extracted from the aerogel for study.

The Track 25 samples have attracted much attention because preliminary examination (Zolensky et al. 2006) showed that they have very low volatile element contents, are FeO-free with compositions dominated by CaO, MgO, Al_2O_3, and SiO_2 (the CMAS oxides) plus minor amounts of Ti-rich phases. They contain phases that are not only characteristic of some types of refractory inclusions found in carbonaceous chondrites, but that also occur in rare refractory IDPs (Zolensky 1987). Refractory IDPs and inclusions consist of minerals that condensed at high temperatures, and identification of the present sample as a Ca-, Al-rich inclusion (CAI) would have important implications for transport of materials from the inner to the outer solar nebula early in the history of the Solar System (Brownlee et al. 2006). Preliminary work has also revealed variations in mineralogy among the Inti particles, requiring comprehensive study of more than one particle, and multiple ultramicrotomed (70-100 nm) thin slices of each particle, for a full understanding of the samples. We have conducted a detailed, multi-disciplinary study of these particles, and herein we document their features in order to determine how similar the original, pre-impact particle might have been to any of the known types of CAIs.

ANALYTICAL METHODS

A small piece of aerogel removed from the Stardust collector and containing Track 25 was flattened between two glass slides. This serves to make the aerogel more easily handled without breaking and to reduce the volume containing the cometary material in preparation for ultramicrotomy (below). After examination with an optical microscope, the terminal particle Inti and two sub-terminal particles, Inti-B and –C, were removed by cutting 200 – 300 μm-sized squares around each particle and embedding with acrylic resin, forming 1 cm-high cylindrical potted butts, following the method of Matrajt and Brownlee (2006). The particles were trimmed with glass knives into stair-step mesas with top squares approximately 100 μm on a side, followed by microtoming with a Leica Ultracut S ultramicrotome using a 45-degree diamond knife to generate thin sections floating in a water-filled boat. Multiple ~70–100 nm-thick microtomed sections were removed from the boat and placed onto 10 nm-thick carbon thin-films supported by 200-mesh Cu or Au TEM grids.

In support of TEM (transmission electron microscope) studies at the University of Washington, after coating with Pd, backscattered electron images of the potted butts of the

terminal particle and both sub-particles were taken with a JEOL JSM 7000F field-emission scanning electron microscope (SEM) operated at 10 kV. All samples were examined with a 200 kV Tecnai F20 field-emission scanning transmission electron microscope (STEM) equipped with a Gatan 2000 energy filter and a light element EDAX energy-dispersive X-ray (EDX) detector. STEM imaging was done with high angle annular dark field (HAADF) and secondary electron detectors. For all EDX analyses, the TEM grids were placed into a standard low-background Be double tilt holder and tilted 15° toward the X-ray detector. High-resolution lattice fringe imaging and electron diffraction were used to measure atomic spacings of individual minerals, which were compared to published mineral d-spacings (Bayliss et al. 1980). In the diffraction patterns, both d-spacings and angular measurements between all reflections were used to match patterns. Relative errors of measured d-spacings are believed to be less than 5%. EDX data were collected and quantified with a 30 mm^2 EDAX light-element detector with embedded Tecnai support software or a stand-alone EDAX Genesis EDX system, which was operated in parallel with the embedded Tecnai EDX system. EDX detector energy calibration was done with a Cu and Al thin-film prepared at the University of Washington. The method of Cliff and Lorimer (1975) was used to determine k-factors for all elements by using well-characterized minerals and the NIST SRM 2063a thin-film standard. Where possible, multiple mineral standards were used for measurement of k-factors. Relative errors are less than 5% for major elements and are estimated to be 15 – 20% for minor elements. Oxide weight percents were calculated from atomic percents.

At Chicago, samples were viewed and analyzed with a JEOL JSM-5800 LV SEM equipped with an Oxford/Link ISIS-300 energy-dispersive X-ray analysis system. Imaging was performed at 25 kV and X-ray analyses were collected at 15 kV. Samples were also examined with a Tecnai F30 STEM operated at 300 kV, with a point-to-point image resolution of 0.2 nm, and equipped with a quantitative energy dispersive X-ray analysis system.

At the Lawrence Livermore National Lab (LLNL), a LEO 1560 analytical SEM with a Gemini field emission column and an Oxford EDX detector and a JEOL JSM-7401F high-resolution field emission SEM equipped with an Oxford Inca-250 EDX were both used to analyze the potted butt of the terminal particle. After the samples were carbon-coated, imaging was carried out at voltages of 4 and 10 kV, and EDX maps and spectra were acquired at 10 kV. Transmission electron microscopy was performed using a monochromated 200 kV Tecnai F20 STEM with an HAADF detector, a quantitative EDAX Genesis 4000 EDX detector and a high

energy Gatan imaging filter for imaging and electron energy loss spectroscopy (EELS). All EELS spectra were recorded with a collection angle of 5.6 mrad and a dispersion of 0.1 eV/channel over 2048 channels. The EELS energy resolution is 0.7 eV with an acquisition time of 3 s, and the spatial resolution is ~0.16 nm. The energy shift of each spectrum was calibrated by a reference zero loss peak taken immediately after each core-loss edge.

Oxygen isotope analyses (McKeegan et al. 2006) were made by CAMECA NanoSIMS at LLNL on two ultramicrotomed sections and with the CAMECA ims 1270 ion microprobe at the University of California, Los Angeles, on the remainder of the acrylic-mounted sample. For the latter analyses, the mesa with the potted butt was cut off and pressed into indium metal in such a manner that the particle was exposed at the surface. The particle was Au-coated and four spots, ~5-10 μm in diameter, were analyzed during two sessions (McKeegan et al. 2006).

Isotopic imaging of oxygen and nitrogen and elemental mapping of carbon, oxygen and nitrogen were performed on two ultramicrotomed sections and the potted butt, respectively, using the CAMECA NanoSIMS 50 ion microprobe at LLNL. Oxygen and nitrogen isotopes were measured simultaneously as $^{16}O^-$, $^{17}O^-$, $^{18}O^-$, $^{12}C^{14}N^-$ and $^{12}C^{15}N^-$ on five electron multipliers at a mass resolving power ~10 000 to resolve all interferences at mass 27 on slices A and B with a ~150 nm Cs^+ beam of 0.8 to 1.1 pA and electron flooding for charge compensation. Slices A and B are two ~100 nm-thick, adjacent sections previously analyzed by transmission electron microscopy and scanning electron microscopy. They consist, respectively, of one fragment about 1 × 1.5 μm in size and four fragments, about 500 nm in size, from a particle originally ~2 × 1.5 μm and embedded in compressed aerogel. Having a known oxygen isotopic composition (McKeegan et al. 2006, supplementary information), aerogel was used as an internal O-isotope standard within each image. Additional matrix effects between aerogel and Inti minerals were corrected using the matrix effect determined by NanoSIMS between aerogel and Wild 2 Mg-rich silicates assuming the latter have the isotopic composition of olivine from another Stardust sample measured by ims 1270 (McKeegan et al. 2006, supplementary information). Nitrogen isotopic analysis proved to be unsuccessful due to the enormous amount of N contamination from the surrounding acrylic; thus, only O isotopes are reported here. Elemental mapping of $^{12}C^-$, $^{16}O^-$ and $^{12}C^{14}N^-$ was performed at high mass resolving power with a ~100 nm Cs^+ beam of 0.53

pA and electron flooding for charge compensation on the potted butt, using a 15-μm raster size to map the entire particle and a 7-μm raster size to map the region containing Ti-rich grains. Pre-sputtering was performed until all N significant contamination was removed. Strong topography effects associated with preferential emission of secondary ions along the boundaries of the grains resulted in contrasted images at grain boundaries. $^{12}C^-$ images were used to map the distribution of residual acrylic in the grain. Image processing was done using software developed by L. R. Nittler.

RESULTS

Petrography and Mineralogy

Terminal Particle

We examined ultramicrotomed slices of the terminal particle, Inti, by SEM and TEM, and we also studied the potted butt by SEM and NanoSIMS elemental mapping. A backscattered electron (BSE) image of the potted butt is shown in Fig. 2a. This image was collected at a moderate accelerating voltage (4 kV), and surface topographic features are evident in addition to features due to atomic number (Z) contrast. Chipping or pitting from ultramicrotomy is visible on the surface, but additional, smooth-sided cavities are present in the interior of the particle, some of which cannot be attributed to ultramicrotome damage or to plucking of material. The particle has an irregular shape and is ~15 × 10 μm across.

During the capture process, aerogel is compressed by impact of the incoming particle and is locally melted by shock and frictional heating. As a result, compressed aerogel and thin rims of solidified impact melt may be seen in the sections. We attempted to identify phases by EDX analysis in the SEM, but in most cases the grain sizes are smaller than the excitation volume of the electron beam of the SEM, so few single-phase spectra could be obtained. Within the area labeled “Ca-Al-Mg silicates with varying compositions”, we obtained spectra consistent with aluminous diopside and spectra with Al>Si, suggesting a spinel component.

A BSE image of the same particle after additional slices were removed by ultramicrotome is shown in Fig. 2b. Some material was plucked and lost (right), but, with greater

Z contrast due to higher accelerating voltage, textural features can be seen here that are not apparent in Fig. 2a. The relatively dark, Al-rich areas in Fig. 2b have Al>Si and probably contain spinel, and the spectra of the Al-poor areas are consistent with low-Al diopside. The bright, Ti-rich spots also contain Ca and are probably perovskite. The two rounded regions in the upper part of Fig. 2b, with Al-rich, low-albedo material enclosed in high-albedo material, could be spinel enclosed in aluminous diopside, an assemblage found in many refractory inclusions. It is important to note that the silicates and oxides are FeO-free, and that no olivine is present in the sample.

These inferences as to mineral identifications as a function of location are supported by TEM analyses, as shown below. Textural relationships can be modified by movement of brittle grain fragments during ultramicrotomy. Thin slices bend by ~45 degrees as they are cut off a sample and silicates usually break into elongated thin fragments. As a result there is often not a direct correlation between microtomed sections and the corresponding potted butt, whose surface is usually undisturbed and similar in appearance to a polished surface.

The area between the two rounded upper regions and the main particle contains glassy material with Fe-metal and sulfide beads. This is most likely compressed and melted-and-quenched aerogel that incorporated cometary sulfide upstream in the track and lodged in the crevices of the particle during deceleration.

High-magnification views, EDX analyses by TEM, and electron diffraction patterns were obtained from ultramicrotomed slices of the particle. At magnifications of 5000×, and even at 20,000-30,000×, all of the sections look texturally similar to each other. This is because the ultramicrotoming process tends to shatter the particles, so that the slices available for study mostly consist of shards (Fig. 3a), obscuring the original shapes of the grains and their textural relationships. At higher magnifications, individual crystals can be readily discerned. An example, shown in Fig. 3b, is a spinel grain at the edge of a silicate shard in the terminal particle. The mineral assemblages vary from slice to slice, which is not surprising for such fine-grained samples.

In another slice, shown in Fig. 4, a mineral assemblage typical of many coarse-grained refractory inclusions found in CV3 carbonaceous chondrites is seen. Fig. 4a, a high angle annular dark-field (HAADF) STEM image, shows compressed (upper left) and vesicular, melted-and-quenched (lower right) aerogel adjacent to the sample, as well as shards and plucked areas due to

ultramicrotoming. The area outlined in Fig. 4a is shown at higher magnification in Fig. 4b, where individual crystals and crystal fragments can be seen. A very important feature of Inti is that it contains Al-rich melilite, occurring as either natural laths or shards (resulting from ultramicrotoming) ~0.5 μm in length (Fig. 4c). We obtained energy-dispersive spectra and a diffraction pattern that are consistent with gehlenite. The d-spacings obtained by electron diffraction are given in Table 1 along with d-spacings from a standard powder pattern for gehlenite. The agreement is very good, to within ~2%. No other Ca-, Al-silicates have similar spacings. In addition, single-crystal data were obtained by selected area electron nano-diffraction. The patterns (Fig. 4d) show a d-spacing of 7.7Å, and the angular relationships between diffraction spots are consistent with a phase having tetragonal symmetry. These features are consistent with melilite, as are the chemical data obtained by EDX (see below). The melilite is adjacent to anorthite and diopside, and closely associated with spinel and aluminous, Ti-bearing clinopyroxene. All of these phases are FeO-free, as in unaltered refractory inclusions. The presence of melilite is highly suggestive of a link to CAIs; in meteorites, this phase only occurs in refractory inclusions.

The FeO-free, Ca-rich pyroxene is another important phase. In Inti and in refractory inclusions, it ranges in composition from pure diopside through aluminous diopside to Ti-, Al-rich clinopyroxene. In Inti, it occurs as subhedral to anhedral, equant grains. In Figs. 4b and 4c, nearly pure diopside appears to be in contact with gehlenite, but this is most likely a superposition of overlying microtome shards. Fig. 5a shows a grain of Ti-rich pyroxene and its EDX spectrum, and Fig. 5b shows Ti-rich pyroxene and Mg-, Al-rich spinel, a phase found in almost all refractory inclusions. Yet another mineral that occurs in Inti and is a primary phase in refractory inclusions is anorthite. It occurs here as anhedral grains, like the one in the bright field image in Fig. 5c.

Round, Ti-rich nuggets ~0.5 μm across can be seen in the BSE image of the potted butt (Fig. 2b). Secondary ion mapping by NanoSIMS (Fig. 6) shows that these grains contain O and do not contain C or N. Analysis by EELS also shows that they are N-free. TEM/EDX analysis of Ti-, Ca-rich grains in ultramicrotomed sections yields spectra with Ca and Ti in ~1:1 atomic proportions, and crystal lattice spacings of 0.27 nm are observed, consistent with perovskite, $CaTiO_3$, yet another phase commonly found in CAIs. It is likely that the Ti-rich nuggets seen by SEM are perovskite as well.

In some of the ultramicrotomed slices, rounded Ti-, V-rich nuggets ~40 nm across are found as inclusions in anorthite and spinel. Electron energy loss spectra (EELS) analysis indicates the presence of N (Zolensky et al. 2006; Chi et al., in prep.) in these inclusions. These features, along with the crystal structure determined by electron nano-diffraction, identify the phase as osbornite, nominally TiN. Osbornite is rare in meteorites, but it has been found intergrown with Mg-Al spinel in a clast in the ALH85085 CH chondrite (Weisberg et al. 1988) and in a refractory inclusion from the Isheyevo (CH/CB) meteorite (Meibom et al. 2007). In the latter inclusion, the V content of the osbornite is below the detection limit of the electron microprobe, and it occurs with grossite ($CaAl_4O_7$), spinel, melilite, and aluminous diopside. In these meteoritic occurrences, the osbornite grains are significantly larger, ~10-25 μm across, than in Inti. Osbornite also occurs in enstatite chondrites and aubrites (Brearley and Jones 1998), meteorites that reflect highly reducing formation conditions.

Elemental mapping of the potted butt by NanoSIMS, however, did not show evidence of any N-rich mineral (Fig. 6), despite the strong ion yield of nitrogen in nitride. This indicates absence of osbornite at the surface of the potted butt. From the analyzed surface area, a maximum concentration of 30 ppm/surface can be estimated for 40 nm osbornite grains.

Metal alloy (FeNi) inclusions are also present in Inti but are even rarer than nitrides (Brownlee et al. 2008). In some cases, the metal is associated with Ti-nitride (e.g. Fig. 4b). The metal grains in Inti are subhedral and up to 80nm across. This is the only Fe-bearing phase found in Inti.

Sub-terminal particles

The two lowermost sub-terminal particles, Inti-B and Inti-C (Fig. 1), were also investigated as part of this study, though not as extensively as the terminal particle, Inti. Like Inti, Inti-B and -C mainly consist of FeO-free, Ca-, Al-rich silicates and spinel. Ultramicrotomed slices and the potted butts of Inti-B and –C were studied. A BSE image of the Inti-B potted butt is shown in Fig. 7a. The particle is 6.1 × 3.7 μm, somewhat smaller than Inti. Like that of Inti, the surface of Inti-B is unevenly pitted by ultramicrotoming, probably due to blade chatter and surface mineralogical variations. Like the terminal particle, Inti-B is too fine-grained for spectra of single phases to be obtained by SEM. Most of the EDS spectra collected from the potted butt of Inti-B are consistent with mixtures of spinel and diopside. These phases, along with anorthite and Ti-rich pyroxene, are shown in Fig. 7b, a representative HAADF image of an

ultramicrotomed slice of the particle. Melilite has not been found in Inti-B. Figure 7c shows a triple junction between anorthite and two grains of diopside, and Fig. 7d shows a spinel grain. Small, Ti-, V-rich grains were also found in Inti-B.

Inti-C is 5.3 × 3.2 μm and is mineralogically similar to Inti-B, mainly consisting of diopside, Ti-rich pyroxene, anorthite and spinel, but no melilite.

Mineral Chemistry

We performed quantitative energy-dispersive analysis in conjunction with both SEM and TEM imaging. It was challenging in many samples to obtain high-quality, quantitative analyses of single minerals within the particles due to the fine-grained nature of the samples and to overlap of grains and aerogel that have been relocated by ultramicrotomy in the ultramicrotomed sections. Selection of grains apparently clear of overlapping grains and aerogel allowed good diffraction patterns and relatively pure, electron beam-induced X-ray spectra to be obtained.

Melilite

Spectra were obtained from the grains shown in Fig. 4c and from other samples of the terminal particle. In all analyses, CaO contents are slightly lower than expected for melilite, and åkermanite contents calculated from Si contents are higher than those obtained from the corresponding Mg and Al contents, probably due to Si X-ray signals from small amounts of aerogel that may have been moved from the periphery to the interior of the sample by ultramicrotomy. Analyses are given in Table 2, and those in which the åkermanite content calculated from the Mg cation abundance, Åk(Mg), agrees with that calculated from the Al cations, Åk(Al), have compositions ~$Åk_5$. The Al/Ca ratios are not affected by aerogel contamination, and in those analyses with good Mg-Al agreement, this ratio is very close to 1, as expected for melilite that is near-end-member gehlenite. The ideal composition of $Åk_5$ is shown in Table 2 for comparison, and the similarity to the low-Åk Inti analyses is evident. Slightly more magnesian compositions, $Åk_{\sim 15\text{-}20}$, quite commonly seen in CAIs, are also found in Inti (Table 2).

Clinopyroxene

In the present samples, this phase is much more abundant than melilite, and it has a wide composition range. Coarse-grained refractory inclusions from CV3 chondrites contain Ti-, Al-

rich clinopyroxene, termed "fassaite" by Dowty and Clark (1973), who showed that it contains both Ti^{3+} and Ti^{4+}. One of the goals of this study is to determine if the Ti-bearing pyroxene (tpx) in Inti has compositions that are within the range of those in CAIs containing Ti^{3+}, which would justify its being called "fassaite" and strengthen the link between Inti and CAIs that formed in the solar nebula and are found in meteorites. Compositions obtained by TEM/EDX range from nearly pure diopside through aluminous diopside to Ti-, Al-rich compositions with 12-17 wt% TiO_2^{tot} (all Ti reported as TiO_2), richer in Ti than most of the fassaite in Type B inclusions and within the range of that in compact Type A CAIs (Simon et al. 1999). Representative analyses of each type of pyroxene in Inti are given in Table 3.

Compositions of Inti diopside and Ti-bearing pyroxene (analyses with 3.91-4.05 cations per six oxygen anions) are compared with those of fassaite from representative Type A and Type B Allende inclusions in Fig. 8. As Fig. 8a shows, MgO and SiO_2 are strongly correlated in fassaite in CAIs, and the trend can be extrapolated to pure diopside at ~55 wt% SiO_2. This reflects the coupling of MgO and SiO_2 in the diopside component ($CaMgSiO_6$) of fassaite. Analyses of Inti Ti-rich pyroxene (tpx) plot on or above the well-defined CAI trend. In fassaite from CAIs, MgO is anticorrelated with TiO_2^{tot} (all Ti reported as TiO_2). On a plot of MgO *vs.* TiO_2^{tot} (Fig. 8b), there is a slight offset between the trends of Type A and Type B fassaite, and Inti tpx compositions mimic the small degree of scatter seen in the Type A compositions. On a plot of Al_2O_3 *vs*. TiO_2^{tot} (Fig. 8c), there is a more pronounced offset between the Type A and Type B fassaite compositions, and Inti tpx compositions either plot on an extension of the Type B trend or overlap with compositions of fassaite from Type A inclusions.

In most of the fassaite found in refractory inclusions, a significant proportion of the Ti is trivalent. This is known directly from optical spectroscopy (Dowty and Clark 1973) and X-ray absorption near-edge structure (XANES) spectroscopy (Simon et al. 2007), and indirectly by calculation of Ti^{3+} proportions necessary for normalization of electron probe analyses to exactly four cations per six oxygen anions (Beckett 1986; Simon et al. 1991, 2007). In the present study, these methods could not be used because of the very fine grain size of the sample, and another technique was used instead: electron energy loss spectroscopy (EELS). Over 15 EELS spectra were collected by Chi et al. (in prep.). A typical EELS spectrum obtained in that work for Inti pyroxene is shown in Fig. 9, along with that for a sample of fassaite from an Allende Type B2 CAI. The spectrum of the Inti pyroxene is remarkably similar to that of the Allende reference

material, which has $Ti^{3+}/(Ti^{3+} + Ti^{4+})$ ~0.66. Thus Inti Ti-rich pyroxene has a significant Ti^{3+} component, probably well within the range of fassaite from Allende Type B inclusions, most of which has $Ti^{3+}/(Ti^{3+} + Ti^{4+})$ between 0.3 and 0.8 (Simon and Grossman, 2006).

The presence of Ti^{3+} in Inti tpx is also indicated by low cation totals (per six oxygen anions), with all Ti reported as Ti^{4+}, as in the analyses shown in Table 3. If Ti^{3+} is present but ignored in calculating the pyroxene formula, too much oxygen is assigned to the measured Ti, and a low cation/anion ratio is derived.

To maintain charge balance when substituting for a divalent cation, such as Mg, Ti enters fassaite via a coupled substitution, typically with one Al cation replacing one Si in a tetrahedral site for substitution of Ti^{3+}, or two Al for two Si with substitution of Ti^{4+}. We can infer the distribution of Al cations between the tetrahedral and octahedral sites from an analysis, assuming there are two tetrahedral cations per six oxygen anions. For each analysis, the number of Al cations necessary to give Al + Si = 2 (per six oxygen) is assigned to the tetrahedral site (^{IV}Al), and the remaining Al is assigned to the octahedral M1 site (^{VI}Al). Due to the coupled substitutions described above, tetrahedral Al abundances should correlate with Ti content, as was observed in Allende fassaite by Simon et al. (1991), who also found that octahedral Al decreases with increasing Ti content. These systematics are also observed for the analyses of Inti pyroxene (Fig. 8d), though a few are displaced from the CAI trends because of their higher tetrahedral Al:Ti cation ratios. This could mean that the Inti fassaite has slightly lower Ti^{3+}/Ti^{4+} ratios than Allende fassaite having the same TiO_2^{tot}.

Ti-free clinopyroxene, i.e. diopside, is more abundant than fassaite in the present samples and is found in many of the microtomed slices of Inti. Its Al_2O_3 contents range from below the EDS detection limits up to ~17 wt%. Aluminous diopside is also commonly found in refractory inclusions, as either a primary or a secondary phase.

Other phases

Anorthite has near-end-member compositions, with ≤ ~0.4 wt% Na_2O. Like unaltered Mg-Al spinel in refractory inclusions, that in Inti is FeO-free. Unlike CAI spinel, however, that in Inti contains ~1 wt% Cr_2O_3. The grains we analyzed contain from 0.6-1.7 wt% Cr_2O_3, and the average Cr_2O_3 content is 1.2 wt%. The grains of osbornite, (Ti,V)N, exhibit a wide range of V contents, from nearly V-free to one with V>Ti, 26.9 *vs.* 23.9 at%. Many grains have solar Ti/V

ratios, ~8 (Anders and Grevesse 1989). Metal in Inti is Ni-poor, with an atomic Fe/Ni ratio of 31. Like metal in many CAIs, it is rich in refractory siderophile elements. A grain in Inti analyzed by Brownlee et al. (2008) contains 2.9 wt% Ni, 2.1% Pt, 1.4% Os, 1% Ir, 0.9% Ru and a 15-nm inclusion of a Mo-, W-rich phase. This represents enrichments of ~1-3 × 10^4 relative to CI chondrites (Anders and Grevesse 1989), levels comparable to those seen in opaque assemblages in CAIs from CV3 chondrites (e.g., Sylvester et al. 1990).

Oxygen Isotopic Compositions

The oxygen isotopic composition of Inti was determined by ion probe analysis of the potted butt and of ultramicrotomed sections of the terminal particle. NanoSIMS analysis indicates that the particle is ^{16}O-enriched, albeit with relatively large uncertainties. No extreme compositions, like those of presolar grains, for example, were detected in Inti. Relatively higher precision analyses were made with the ims 1270 at UCLA. These analysis spots, three of which are indicated in Fig. 2b, were larger than the grain size, so the data represent the bulk isotopic composition of the particle. These data, given in Table 4 and illustrated in Fig. 10, clearly show that Inti is ^{16}O-rich relative to terrestrial oxygen, with all analyses plotting within error of the carbonaceous chondrites anhydrous minerals mixing line (CCAM) at $\delta^{17}O \approx \delta^{18}O \approx -40‰$. This is more ^{16}O-rich than most bulk CAIs, but very close to the compositions of the most ^{16}O-rich, unaltered components of refractory inclusions from carbonaceous chondrites (Clayton et al. 1977; McKeegan and Leshin 2001; Yurimoto et al. 2008). In most large CAIs from CV chondrites, melilite and anorthite are typically less ^{16}O-rich, at ~-20 to 0‰ (Clayton et al. 1977; McKeegan and Leshin 2001; Krot et al. 2002), than pyroxene and spinel, a pattern which is thought to result from isotopic exchange with a relatively ^{16}O-poor gas or (possibly) fluid. Many spinel, hibonite and even some fassaite grains in coarse-grained (e.g., Clayton et al. 1977; McKeegan and Leshin 2001; Krot et al. 2002) and fine-grained (Aléon et al. 2002; Fagan et al. 2004; Itoh et al. 2004) meteoritic CAIs are commonly found to have O-isotopic compositions between -40‰ and -50‰. Even more extreme compositions have been found in some very rare chondrules (Kobayashi et al. 2003).

The mineralogical control of oxygen isotopic composition is typically not seen in many smaller CAIs, which tend to be isotopically homogeneous, and in this respect Inti is like other

small CAIs and the refractory IDPs; as shown in Fig. 10, the Inti analyses are also similar to the compositions of two refractory IDPs (McKeegan 1987). Many CAIs from ordinary and enstatite chondrites, which are smaller than those from CVs but are probably still significantly larger and coarser-grained than Inti, also show ^{16}O-enriched compositions of $\delta^{17}O \approx \delta^{18}O \approx -40‰$ (Fagan et al. 2001; Guan et al. 2000; McKeegan et al. 1998). In contrast, the vast majority of chondrules, whether from ordinary or carbonaceous chondrites, are much poorer in ^{16}O than either Inti or CAIs (Clayton et al. 1991). It is clear that Inti, like other small CAIs, could not have interacted at high temperature with a gas of similar isotopic composition as that which was present during chondrule formation.

DISCUSSION

What did Inti look like pre-impact?

As the comet particles decelerated in the aerogel they tended to leave trails of material along the tracks they created, and Inti was no exception (Fig. 1). To truly assess the composition of the particle prior to impact into aerogel would require analysis of particles along the entire length of the track and distinguishing additional fragments of Inti from materials petrologically unrelated to Inti, and that is beyond the scope of this paper. The two sub-terminal particles we studied are clearly related to Inti, but we do not know whether they are from the original exterior of the inclusion or from its interior, or how large the inclusion originally was. Assuming Inti and at least the four largest sub-terminal particles were originally one object, the original particle could have been ~30 μm across, and uniformly fine-grained. It might also have been zoned with respect to the distribution of minerals, as gehlenite has been found in Inti but not in the sub-terminal particles. Analyses of additional sub-particles could, however, significantly modify the inferred modal mineralogy of Inti.

Is Inti a refractory inclusion from the solar nebula?

A comparison of the features of the Track 25 particles with those of refractory inclusions found in meteorites shows similarities and differences. The main difference is that Inti *appears*

to be much finer-grained than meteoritic CAIs of similar mineralogy. Observation of samples by TEM shows grain sizes ~0.5 μm, but this must be taken as a lower limit to the original grain size range, because ultramicrotoming shatters the rock surfaces, breaking grains into shards and commonly tumbling them so that they are not in their original arrangements in an ultramicrotomed slice. Some discrete, *in situ* sub-micron grains can be discerned, such as the spinel grain shown in Fig. 3b and the pyroxene grains shown in Fig. 7c, but we cannot rule out the possibility that these are off-center sections through larger grains. When we attempted SEM/EDX analysis of the potted butt, we could not obtain clean, single-mineral spectra, which indicates a typical grain size less than ~2 μm. This is our best indication of the grain size of Inti, because the material in potted butt was not microtomed. Many of the grains observed in the ultramicrotomed slices probably were originally somewhat larger; Inti probably has a typical grain size between 1 and 2 μm. This is within the range of fine-grained inclusions, such as those in CO and reduced CV3 chondrites, that contain many of the phases found in Inti, and have O-isotopic compositions within error of the Inti composition (Itoh et al. 2004; Fagan et al. 2004). In addition, μm-sized perovskite and spinel can be found in coarse-grained CAIs (e. g., Hutcheon 1977). Thus, we do not consider the grain size of Inti to be a feature outside the range seen in meteoritic CAIs.

The mineralogic and isotopic similarities between Inti and CAIs are striking. The inventory of phases present in the Track 25 particles, their chemical compositions and the oxygen isotopic composition of Inti provide strong evidence that the present samples are related to refractory inclusions found in meteorites, and thus formed in the solar nebula. It seems highly unlikely that the similarities are fortuitous. Both Inti and CAIs consist of Ca-, Al-rich, FeO-free, ^{16}O-rich phases. Major phases that Inti has in common with CAIs are anorthite, spinel, Ti-rich fassaite, and aluminous diopside. Based on the samples examined thus far, melilite is probably a minor phase in Inti, but its presence is important because it is a primary phase in many refractory inclusions. It is a major phase in most CAIs in CV3, CH and CO chondrites, and also occurs, but less commonly, in inclusions from CM chondrites (Brearley and Jones 1998). Perovskite is also a minor phase in Inti and is found in most Type A inclusions (Grossman 1980), and in many inclusions in CM2 chondrites (Brearley and Jones 1998).

It is important to note that all of these phases are predicted to condense at high temperatures, from 1688K (perovskite) to 1416K (anorthite), from a cooling gas of solar

composition at a total pressure of 10^{-3} atm (Yoneda and Grossman 1995), although this does not mean that Inti formed this way. In addition to condensate refractory inclusions, those that solidified from liquids also consist of these phases. Solidified melts tend to be more compact than aggregates of gas-solid condensate grains. The views of the potted butts show that Inti is fairly compact, unlike the porous inclusions that are the most likely examples of condensates, such as "fluffy" Type A inclusions and the Murchison inclusion SH-6 (MacPherson and Grossman 1984; MacPherson et al. 1984). The presence of a triple junction in Inti-B (Fig. 7c) also suggests that Inti is not a pristine condensate.

Osbornite requires formation conditions quite different from those inferred for the commonly observed refractory phases, so their coexistence is somewhat puzzling. Condensation calculations show that the stabilities (and condensation temperatures) of nitrides and carbides increase with increasing C/O in a gas that is otherwise of solar composition. The solar C/O ratio is 0.5 (Allende Prieto 2002), and an increase by a factor of ~2 is necessary to stabilize carbides and nitrides (Grossman et al. 2008). Equilibrium condensation of TiN only occurs over a very narrow range of C/O ratios, ~0.96-0.98 (Ebel 2006). Any Ti-bearing pyroxene formed in such an oxygen-poor environment would have a vanishingly small Ti^{4+} content, however, unlike that in Inti. The Ti-rich fassaite in Inti has a Ti^{3+}/Ti^{4+} ratio like that of typical Allende fassaite; the presence of Ti^{3+} in Inti points to formation under reducing conditions, probably similar to those recorded in meteoritic CAIs (Beckett 1986; Grossman et al. 2008). Inti either formed in the nebula that gave rise to our Solar System, or in some other nebula of similar chemical and isotopic composition.

In its occurrences in Isheyevo (Meibom et al. 2007) and in Inti, osbornite is enclosed in "normal" refractory phases (grossite and melilite in Isheyevo, spinel in Inti). Perhaps there were local C-enriched regions of the nebula where osbornite formed, was transported to a region where CAIs formed, and became enclosed in condensates from a gas of solar composition before it could be destroyed by reaction with the nebular gas.

Interpretation of the observations of Inti is analogous to the comparison of refractory IDPs with CAIs from meteorites. Several IDPs have been found that consist of the CMAS oxides plus TiO_2. One is spinel- and pyroxene-rich (Christoffersen and Buseck 1986) and the others consist of hibonite, melilite and perovskite (Zolensky 1987). Thus, like Inti, they are composed of phases that are equilibrium high-temperature condensates from a gas of solar composition. As

reported by (McKeegan 1987), the IDPs described by Zolensky (1987) have ^{16}O-rich isotopic compositions that are similar to those of primary phases in CAIs (McKeegan 1987). In addition, as shown in Fig. 10, those IDPs are also isotopically similar to Inti. With most grains ≤0.2 μm across, however, the refractory IDPs are much finer-grained than most meteoritic CAIs. Zolensky (1987) and McKeegan (1987) therefore concluded that refractory IDPs were not derived from samples of the known meteorite suite, and that they represent a new class of extraterrestrial material.

That conclusion was based on true grain size differences, as the IDPs were not microtomed, and a similar conclusion is not reached here. Inti can be considered to be a type of fine-grained refractory inclusion (FGI). In fact, although most FGIs are spinel-rich and pyroxene-poor compared to Inti (e.g., Krot et al. 2004), and they tend to contain Al-diopside rather than fassaite, at least one FGI is known that basically has the same mineralogy as Inti. Reported by Krot et al. (2004), it was found in Leoville and consists of spinel, anorthite, perovskite, melilite, Ti-rich pyroxene and Al-diopside, with an olivine-rich accretionary rim. The oxygen isotopic composition of that sample has not been measured, but primary phases in many other FGIs typically have δ^{17}O, δ^{18}O between -50 and -40‰ (Aléon et al. 2002; Itoh et al. 2004; Fagan et al. 2004), within error of the composition of Inti.

Transport of CAI material from hot inner nebular regions to the outer solar nebula

Having characteristics typical of most CAIs, Inti probably formed in an 16O-rich region of the inner solar nebula in a high-temperature, reduced, water-free environment. Therefore, its presence in a short period comet requires transport over 10's of astronomical units to the outer, cold nebular regions of comet formation (Levison and Morbidelli 2003), as previously emphasized by McKeegan et al. (2006). Transport outward over such large distances in an (inward flowing) accretion disk requires an efficient mechanism. A bipolar outflow, such as proposed in the X-wind model (Shu et al. 1997), is one possible way of sending a small CAI from the inside edge of the accretion disk to the outermost nebula and, in fact, the presence of CAIs in comets was a prediction of the model (Shang et al. 2000). Another mechanism that has been advocated for radial transport outward in the solar nebula is turbulence (e.g., Bockelée-Morvan et al. 2002; Ciesla 2007). Two-dimensional simulations of viscously-evolving disks

have shown that an ~15 micron CAI can be transported outward via turbulence over 10-20 astronomical units on timescales of 10^5 years (Ciesla 2007). This requires mass transport rates through the disk of $\sim 10^{-7}$ solar masses per year, which is consistent with the observed rates for disks around young ($<5 \times 10^5$ year-old) T-Tauri stars (Calvet et al. 2005).

Alternatively, formation of Inti in another protostellar nebula with solar-like chemical and isotopic composition requires both an efficient transport mechanism and survival of the interstellar journey. No mineralogical evidence of interstellar irradiation by H or He particles, shocks or galactic cosmic rays (e.g. amorphous regions or nuclear tracks) has so far been found in Inti. If initially present in Inti, however, such evidence may have been erased by gas loss and annealing during impact capture. A detailed understanding of heating effects during impact in aerogel and a systematic search among Inti fragments are needed to evaluate this possibility.

Determination of the ^{26}Al content of Inti is now crucial for estimating the timing and locale of its formation. Deciphering the distribution of ^{26}Al in comets will help us fully understand the origin of ^{26}Al in the early Solar System and elucidate the astrophysical setting of Solar System birth, since only a limited amount of ^{26}Al can be produced by irradiation by solar energetic particles, and negligible amounts of irradiation-induced ^{26}Al are expected to have reached the comet-forming region of the nebula (Duprat and Tatischeff 2007).

CONCLUSIONS

We have conducted a multidisciplinary study of the terminal particle, Inti, and two related sub-terminal particles from Stardust Track 25. There are striking similarities between the present sample and CAIs with respect to mineralogy, mineral chemistry, Ti oxidation state, and oxygen isotopic composition. The particles studied are fine-grained (<~2 μm) and largely consist of FeO-free, Ca-, Al-rich phases that are also found in typical refractory inclusions from carbonaceous chondrites and are predicted to condense at equilibrium from a cooling gas of solar composition. At least one meteoritic fine-grained refractory inclusion is known that has the same mineralogy as Inti, except for osbornite, a mineral which is present in Inti, is very rare in CAIs

and requires a gas with a C/O ratio greater than the solar value for formation by equilibrium condensation.

Inti could have been ejected from a nebula that was both chemically and isotopically similar to the one from which our Solar System formed, but it retains no record of interstellar exposure. It is more likely that it formed in the inner solar nebula and was transported outward to the comet-forming region, either in a bipolar outflow or by turbulence, during the formation of the Solar System.

ACKNOWLEDGMENTS

We thank F. Ciesla for helpful discussions. This work was supported by the National Aeronautics and Space Administration (NASA) through grants NNG05GG00G (LG), NNG05G177G (LG), NNH06AD671 (JPB) and NNH04AB491 (JPB). MC is supported by a SEGRF Fellowship at LLNL. Portions of this work were performed under the auspices of the U. S. Department of Energy by Lawrence Livermore National Laboratory, in part under contract no. W-7405-Eng-48 and in part under Contract DE-AC52-07NA27344. A. Brearley, T. Fagan and two anonymous reviewers provided reviews that led to improvements in the text. We are also very grateful to the Discovery and the Cosmochemistry programs of NASA for funding and supporting the Stardust mission.

REFERENCES

Aléon J., Krot A. N., and McKeegan K. D. 2002. Calcium-aluminum-rich inclusions and amoeboid olivine aggregates from the CR carbonaceous chondrites. *Meteoritics & Planetary Science* 37:1729-1755.

Allende Prieto C., Lambert D. L., and Asplund M. 2002. A reappraisal of the solar photospheric C/O ratio. *Astrophysical Journal Letters* 573:L137-L140.

Anders E. and Grevesse N. 1989. Abundances of the elements: Meteoritic and solar. *Geochimica et Cosmochimica Acta* 53:197-214.

Bayliss P., Berry L. G., Mrose M. E., and Smith D. K. (eds) 1980. *JCPDS Mineral Powder Diffraction File Data Book.* JCPDS International Centre for Diffraction Data, Swarthmore, PA.

Beckett J. R. 1986. The origin of calcium-, aluminum-rich inclusions from carbonaceous chondrites: an experimental study. Ph. D. dissertation, University of Chicago.

Bockelée-Morvan D., Gautier D., Hersant F., Hure J.-M. and Robert F. 2002. Turbulent radial mixing in the solar nebula as the source of crystalline silicates in comets. *Astronomy and Astrophysics* 384:1107-1118.

Bradley J. P. and Brownlee D. E. 1986. Cometary particles: thin sectioning and electron beam analysis. *Science* 231:1542-1544.

Brearley A. J. and Jones R. H. 1998. Chondritic meteorites. In *Planetary Materials, Reviews in Mineralogy Vol. 36*, edited by Papike J. J. Washington, D.C.: Mineralogical Society of America. pp. 3-1 - 3-398.

Brownlee D. E., Joswiak D. J., Schlutter D. J., Pepin R. O., Bradley J. P., and Love S. G. 1995. Identification of individual cometary IDPs by thermally stepped He release. *Lunar and Planetary Science* XXVI:183-184.

Brownlee D. E. and 182 others. 2006. Comet 81P/Wild 2 under a microscope. *Science* 314:1711-1716.

Brownlee D. E., Joswiak D., Matrajt G., Bradley J., and Ebel D. S. 2008. Ultra-refractory attogram inclusions in comet dust – First condensates? *Lunar and Planetary Science* XXXIX:1978.

Calvet N., Briceño C., Hernández J., Hoyer S., Hartmann L., Sicilia-Aguilar A, Megeath S. T., and D'Alessio P. 2005. Disk evolution in the Orion OB1 association. *Astronomical Journal* 129:935-946.

Christoffersen R. and Buseck P. R. 1986. Refractory minerals in interplanetary dust. *Science* 234:590-592

Ciesla F. J. 2007. Outward transport of high-temperature materials around the midplane of the solar nebula. *Science* 318:613-615.

Clayton R. N., Onuma N., Grossman L., and Mayeda T. K. 1977. Distribution of the presolar component in Allende and other carbonaceous chondrites. *Earth and Planetary Science Letters* 34:209-224.

Clayton R. N., Mayeda T. K., Goswami J. N., and Olsen E. J. 1991. Oxygen isotope studies of ordinary chondrites. *Geochimica et Cosmochimica Acta* 55:2317-2337.

Cliff G. and Lorimer G. W. 1975. The quantitative analysis of thin specimens. *Journal of Microscopy* 103:203-207.

Dowty E. and Clark J. R. 1973. Crystal structure refinement and optical properties of a Ti^{3+} fassaite from the Allende meteorite. *American Mineralogist* 58:230-242.

Duprat J. and Tatischeff V. 2007. Energetic constraints on in situ production of short-lived radionuclei in the early solar system. *Astrophysical Journal* 671:L69-L72.

Ebel D. S. 2006. Condensation of rocky material in astrophysical environments. In Meteorites and the Early Solar System II, edited by D. S. Lauretta and H. Y. McSween, Jr. Tucson, AZ. The University of Arizona Press. pp. 253-277.

Fagan T. J., McKeegan K. D., Krot A. N., and Keil K. 2001. Calcium-aluminum-rich inclusions in enstatite chondrites (II): Oxygen isotopes. *Meteoritics & Planetary Science* 36:223-230.

Fagan T. J., Krot A. N., Keil K., and Yurimoto H. 2004. Oxygen isotopic alteration in Ca-Al-rich inclusions from Efremovka: Nebular or parent body setting? *Meteoritics & Planetary Science* 39:1257-1272.

Gounelle M., Spurny P., and Bland P. A. 2006. The orbit and atmospheric trajectory of the Orgueil meteorite from historical records. *Meteoritics & Planetary Science* 41:135-150.

Grossman L. 1980. Refractory inclusions in the Allende meteorite. *Annual Reviews Earth and Planetary Science* 8:559-608.

Grossman L., Beckett J. R., Fedkin A. V., Simon S. B., and Ciesla F. J. 2008. Redox conditions in the solar nebula: Observational, experimental, and theoretical constraints. In: *Oxygen in the Solar System, Reviews in Mineralogy and Geochemistry vol. 68*, edited by MacPherson G. J., Mittlefehldt D. W., Jones J. H. and Simon S. B. Chantilly, VA. Mineralogical Society of America. pp 93-140.

Guan Y., McKeegan K. D., and MacPherson G. J. 2000. Oxygen isotopes in calcium-aluminum-rich inclusions in enstatite chondrites: new evidence for a common CAI source in the solar nebula. *Earth and Planetary Science Letters* 181:271-277.

Hutcheon I. D. 1977. Micro-mineralogy of calcium-aluminum-rich inclusions from Allende. *Lunar Science* VIII:487-489.

Itoh S., Kojima H., and Yurimoto H. 2004. Petrography and oxygen isotopic compositions in refractory inclusions from CO chondrites. *Geochimica et Cosmochimica Acta* 68:183-194.

Kobayashi S., Imai H., and Yurimoto H. 2003. New extreme O16-rich reservoir in the early solar system. *Geochemical Journal* 37:663-669.

Krot A. N., McKeegan K. D., Leshin L. A., MacPherson G. J., and Scott E. R. D. 2002. Existence of an ^{16}O-rich gaseous reservoir in the solar nebula. *Science* 295:1051-1054.

Krot A. N., MacPherson G. J., Ulyanov A. A., and Petaev M. I. 2004. Fine-grained, spinel-rich inclusions from the reduced CV chondrites Efremovka and Leoville: I. Mineralogy, petrology, and bulk chemistry. *Meteoritics & Planetary Science* 39:1517-1553.

Levison H. F. and Morbidelli A. 2003. The formation of the Kuiper belt by the outward transport of bodies during Neptune's migration. *Nature* 426:419-421.

MacPherson G. J. and Grossman L. 1984. "Fluffy" Type A Ca-, Al-rich inclusions in the Allende meteorite. *Geochimica et Cosmochimica Acta* 48:29-46.

MacPherson G. J., Bar-Matthews M., Tanaka T., Olsen E., and Grossman L. 1983. Refractory inclusions in the Murchison meteorite. *Geochimica et Cosmochimica Acta* 47:823-839.

MacPherson G. J., Grossman L., Hashimoto A., Bar-Matthews M., and Tanaka T. 1984. Petrographic studies of refractory inclusions from the Murchison meteorite. *Proceedings of the 15th Lunar and Planetary Science Conference, Journal of Geophysical Research Supplement* 89:C299-C312.

Matrajt G. and Brownlee D. E. 2006. Acrylic embedding of Stardust particles encased in aerogel. *Meteoritics & Planetary Science* 41:1715-1720.

McKeegan K. D. 1987. Oxygen isotopes in refractory stratospheric dust particles: Proof of extraterrestrial origin. *Science* 237:1468-1471.

McKeegan K. D. and Leshin L. A. 2001. Stable isotope variations in extraterrestrial materials In *Stable Isotope Geochemistry, Reviews in Mineralogy and Geochemistry 43,* edited by Valley J. W. and Cole D. R., Washington DC, Mineralogical Society of America, pp. 279-318.

McKeegan K. D., Leshin L. A., Russell S. S., and MacPherson G. J. 1998. Oxygen isotopic abundances in calcium-aluminum-rich inclusions from ordinary chondrites: Implications for nebular heterogeneity. *Science* 280:414-418.

McKeegan K. D. and 46 others. 2006. Isotopic compositions of cometary matter returned by Stardust. *Science* 314:1724-1728.

McSween H. Y. Jr. and Weissman P. R. 1989. Cosmochemical implications of the physical processing of cometary nuclei. *Geochimica et Cosmochimica Acta* 53:3263-3271.

Meibom A., Krot A. N., Robert F., Mostefaoui S., Russell S. S., Petaev M. I., and Gounelle M. 2007. Nitrogen and carbon isotopic composition of the Sun inferred from a high-temperature solar nebular condensate. *The Astrophysical Journal* 656:L33-L36.

Rietmeijer F. J. M. 1998. Interplanetary dust particles. In *Planetary Materials, Reviews in Mineralogy Vol. 36*, edited by Papike J. J. Washington, D.C.: Mineralogical Society of America. pp. 2-1 - 2-95.

Shang H., Shu F. H., Lee T., and Glassgold A. E. 2000. Protostellar winds and chondritic meteorites, formation of solids: the first step. *Space Science Reviews* 92:153-176.

Shu F. H., Shang H., Glassgold A. E., and Lee T. 1997. X-rays and fluctuating X-winds from protostars. *Science* 277:1475-1479.

Simon S. B. and Grossman L. 2006. A comparative study of melilite and fassaite in Types B1 and B2 refractory inclusions. *Geochimica et Cosmochimica Acta* 70:780-798.

Simon S. B., Grossman L., and Davis A. M. 1991. Fassaite composition trends during crystallization of Allende Type B refractory inclusions. *Geochimica et Cosmochimica Acta* 55:2635-2655.

Simon S. B., Davis A. M., and Grossman L. 1999. Origin of compact type A refractory inclusions from CV3 carbonaceous chondrites. *Geochimica et Cosmochimica Acta* 63:1233-1248.

Simon S. B., Sutton S. R., and Grossman L. 2007. Valence of titanium and vanadium in pyroxene in refractory inclusion interiors and rims. *Geochimica et Cosmochimica Acta* 71:3098-3118.

Sylvester P. J., Ward B. J., Grossman L., and Hutcheon I.D. 1990. Chemical compositions of siderophile element-rich opaque assemblages in an Allende inclusion. *Geochimica et Cosmochimica Acta* 54:3491-3508.

Weisberg M. K., Prinz M., and Nehru C. 1988. Petrology of ALH85085: a chondrite with unique characteristics. *Earth and Planetary Science Letters* 91:19-32.

Yoneda S. and Grossman L. 1995. Condensation of CaO-MgO-Al_2O_3-SiO_2 liquids from cosmic gases. *Geochimica et Cosmochimica Acta* 59:3413-3444.

Yurimoto H., Krot A. N., Choi B.-K., Aléon J., Kunihiro T., and Brearley A. J. 2008. Oxygen isotopes of chondritic components. In: *Oxygen in the Solar System, Reviews in Mineralogy and Geochemistry vol. 68*, edited by MacPherson G. J., Mittlefehldt D. W., Jones J. H and Simon S. B. Chantilly, VA. Mineralogical Society of America. pp 141 – 186.

Zolensky M. E. 1987. Refractory interplanetary dust particles. *Science* 237:1466-1468.

Zolensky M. E. and 74 others. 2006. Mineralogy and petrology of Comet 81P/Wild 2 nucleus samples. *Science* 314:1735-1739.

Table 1. Measured d-spacings (Å) in Inti melilite and standard gehlenite.

hkl	Inti[1]	Gehlenite[2]
(100)	7.8	7.7
(001)	5.2	5.1
(101)	4.3	4.2
(201)	3.1	3.1

[1]d-spacings from electron diffraction pattern. [2]d-spacings from X-ray powder diffraction, Cu K_α radiation, JCPDS pattern 20-199.

Table 2. Energy-dispersive (TEM/EDX) analyses of melilite in Inti, with values for $Åk_5$ shown for comparison.

	Inti	Inti	Inti	Inti	Inti	Inti	$Åk_5$
Na_2O	BDL	0.3	0.2	0.4	BDL	BDL	0
MgO	2.4	1.7	1.0	0.6	0.6	0.8	0.74
Al_2O_3	29.2	31.3	34.9	35.5	35.5	35.5	35.33
SiO_2	28.7	26.9	25.2	25.4	25.5	24.5	23.01
CaO	39.7	39.8	38.8	38.1	38.4	39.1	40.91
				Cations per 7 oxygen anions			
Na	0	0.03	0.02	0.04	0	0	0
Mg	0.16	0.12	0.07	0.04	0.04	0.05	0.05
Al	1.55	1.67	1.85	1.88	1.88	1.89	1.90
Si	1.30	1.22	1.14	1.14	1.15	1.11	1.05
Ca	1.92	1.93	1.87	1.84	1.85	1.89	2.00
Total	4.93	4.97	4.95	4.94	4.92	4.94	5.00
Åk(Mg)	16.1	11.5	6.7	4.0	4.0	5.4	5.0
Åk(Al)	22.4	16.5	7.3	5.9	6.0	5.4	5.0
Åk(avg)	19.3	14.0	7.0	5.0	5.0	5.4	5.0

Analyses are normalized to 100 wt% oxides. Relative uncertainties based on counting statistics are ~5% for Al_2O_3, SiO_2 and CaO, ~15% for MgO and Na_2O. Åk(avg) values are averages of the åkermanite (Åk) contents calculated from Mg (Åk(Mg)) and Al (Åk(Al)) cation abundances. BDL: below detection limit.

Table 3. Energy-dispersive (TEM/EDX) analyses of pyroxene in Inti.

Sample	1	2	3	4
MgO (wt%)	18.3	14.7	7.4	6.7
Al_2O_3	3.1	11.8	21.7	24.8
SiO_2	54.4	47.7	31.5	27.8
CaO	24.0	25.4	24.9	24.9
TiO_2	0.2	0.4	14.5	15.7
		Cations per six oxygen anions		
Si	1.948	1.724	1.175	1.044
^{IV}Al	0.052	0.276	0.825	0.956
^{VI}Al	0.079	0.227	0.129	0.142
Mg	0.977	0.792	0.411	0.375
Ti	0.005	0.011	0.407	0.444
Ca	0.921	0.984	0.995	1.002
Total	3.982	4.014	3.942	3.963

Analyses are normalized to 100 wt% oxides. Relative uncertainties based on counting statistics are ~5%. 1: Diopside. 2: Al-diopside. 3, 4: Fassaite.

Table 4. Oxygen isotopic compositions of Inti, determined by ion probe (ims 1270) and NanoSIMS (NS).

Sample	$\delta^{18}O$ (‰)	2σ	$\delta^{17}O$ (‰)	2σ
Inti-1270-1	-39.5	1	-39.4	4.3
Inti-1270-2	-40.9	1.3	-40.5	1.6
Inti-1270-3	-41.6	1.3	-42.0	2.6
Inti-1270-4	-36.1	2.4	-38.7	3.8
Inti-NS	-44	9	-56	15

Figure Captions

Fig. 1 Optical view of Track 25 in aerogel, after removal of the terminal particle from the narrow end of the track. Four major sub-terminal particles are circled, and many particles larger than 2 μm are present. Inti-B and Inti-C (in bold circles) are sub-terminal particles that were included in this study. Track is ~2 mm long.

Fig. 2. Backscattered electron images of the potted butt of Inti, the terminal particle. a) Image showing pitting/plucking of the sample surface due to ultramicrotoming. A low accelerating voltage (4 kV) was used to minimize damage to the embedding medium. b) Same particle after additional sectioning. Two Ti-rich grains have been exposed, but material has been lost by plucking from the embedding medium (right). More detail and contrast can be seen than in a), due to higher accelerating voltage (10 kV). Areas analyzed by ion probe for determination of oxygen isotopic compositions are outlined. Scale bar is 1 μm. After Zolensky et al. (2006) and McKeegan et al. (2006).

Fig. 3. a) Bright field TEM image of a slice of the terminal particle, showing shards of material, compressed aerogel and plucked areas with no grains. b) Bright field TEM image of a silicate shard in a different slice of the terminal particle, containing a spinel grain.

Fig. 4. a) HAADF image of a slice of the terminal particle containing melilite (gehlenite). b) View of area outlined by the box in (a), showing an assemblage of phases that are commonly found in refractory inclusions: anorthite (An); diopside (Di); gehlenite (Ge); spinel (Sp); and Ti-rich clinopyroxene (Tpx). c) Higher-magnification view of melilite laths and adjacent diopside, with representative EDS spectra. Peaks for Cu are artifacts. d) Electron diffraction patterns from the [001] (left) and [010] (right) zone axes of gehlenite in Inti.

Fig. 5. Images of phases in Inti that are common in CAIs. a) HAADF image of a Ti-rich clinopyroxene grain, along with its EDX spectrum. The quantitative analysis derived from this spectrum is given in Table 3. b) HAADF image of Ti-rich pyroxene in contact with spinel, and corresponding EDS spectra. c) Bright field image of anhedral spinel and anorthite in contact.

Fig. 6. Elemental maps of O (a), C (c) and N (d), acquired by NanoSIMS as secondary ion images of $^{16}O^-$, $^{12}C^-$ and $^{12}C^{14}N^-$, respectively, in the largest fragment of the potted butt of Inti. The area mapped is 7 × 7 μm. A BSE image (b) of the area is shown for reference. The brightest regions in the $^{16}O^-$ image correspond to regions with strong ion emission due to topography of the sample (mainly edges of the grain). The carbon and nitrogen signals are dominated by emission from the acrylic embedding medium. In the oxygen map (a), the grains rich in Ti (white outline) are blue, indicating that they have slightly more oxygen than the surrounding material (mostly black) and suggesting that they are probably oxides, which have higher O^- yields than silicates. **Holes are outlined in red[[??]]** for use as location reference points. Note the absence of bright spots in the N-map, indicating the absence of nitrides at the surface of this fragment.

Fig. 7. a) Backscattered electron image of the potted butt of sub-terminal particle Inti-B. Note the similar albedo and texture, with uneven distribution of pitting, as in the terminal particle Inti (Fig. 2). Also, as with the terminal particle, most SEM/EDX point analyses indicate mixtures of phases. Image collected at 10 kV. b) Representative HAADF view of a microtomed slice of Inti-B. c) Bright field (BF) image of a triple junction between two pyroxene grains and an anorthite grain in Inti-B. Scale bar is 100 nm. d) HAADF image of a spinel grain in Inti-B. Spectrum shows it is nearly pure $MgAl_2O_4$ except for ~1 wt% Cr_2O_3.

Fig. 8. Comparison of compositions of pyroxene in Inti to those of fassaite from Types A and B coarse-grained refractory inclusions from Allende. Diopside occurs in refractory inclusions but is not among the Allende analyses shown here. Inti analyses are by TEM/EDX and Allende data are wavelength-dispersive electron probe analyses. a) Wt% MgO *vs.* SiO_2. The correlation between these oxides is stronger in meteoritic fassaite than in the Inti analyses. b) Wt% MgO *vs.* TiO_2^{tot} (all Ti treated as TiO_2). Analyses of Ti-rich pyroxene in Inti overlap with those of fassaite from a representative Allende compact Type A inclusion (TS68). c) Wt% Al_2O_3 *vs.* TiO_2^{tot}. The Ti-rich Inti analyses either plot on an extension of the Type B trend or overlap with the Allende Type A fassaite. d) Al

vs. Ti, cations per six oxygen anions. Inti analyses fit the Allende trend except for a few that are offset to higher tetrahedral Al contents.

Fig. 9. Electron energy loss spectra (counts in arbitrary units) showing the Ti-L2,3 core scattering edge for Inti Ti-rich pyroxene and Allende fassaite with Ti^{3+}/Ti^{4+} ~2. The Inti spectrum is very similar to the Allende spectrum, indicating the presence of Ti^{3+} in the Inti pyroxene. After Chi et al. (in prep.).

Fig. 10. Three-isotope plot of the oxygen isotopic compositions of Inti and refractory interplanetary dust particles (Ref IDPs). Analyses of Inti by two different ion probes (ims-1270 and NanoSIMS) are similar to those of refractory IDPs, and plot within error (2σ) of the carbonaceous chondrite anhydrous minerals (CCAM) mixing line, as do bulk compositions of normal (non-FUN) refractory inclusions. Compositions are relative to Standard Mean Ocean Water (SMOW). The terrestrial fractionation line (TF) and CCAM are shown for reference. IDP data are from McKeegan (1987).

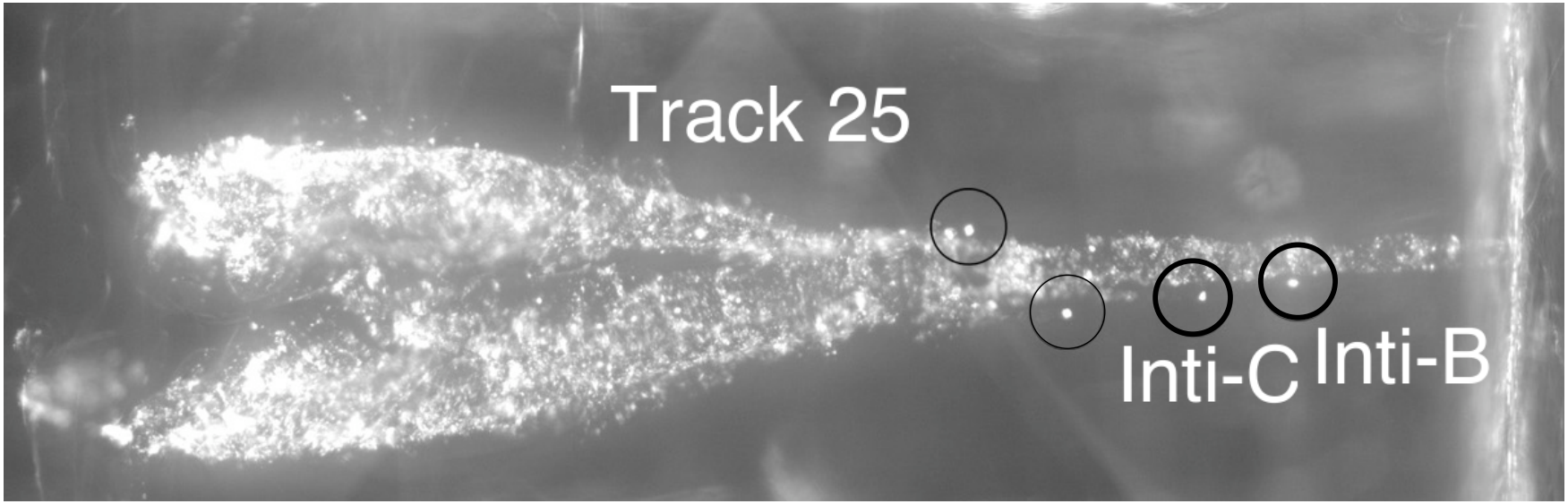

Fig. 1

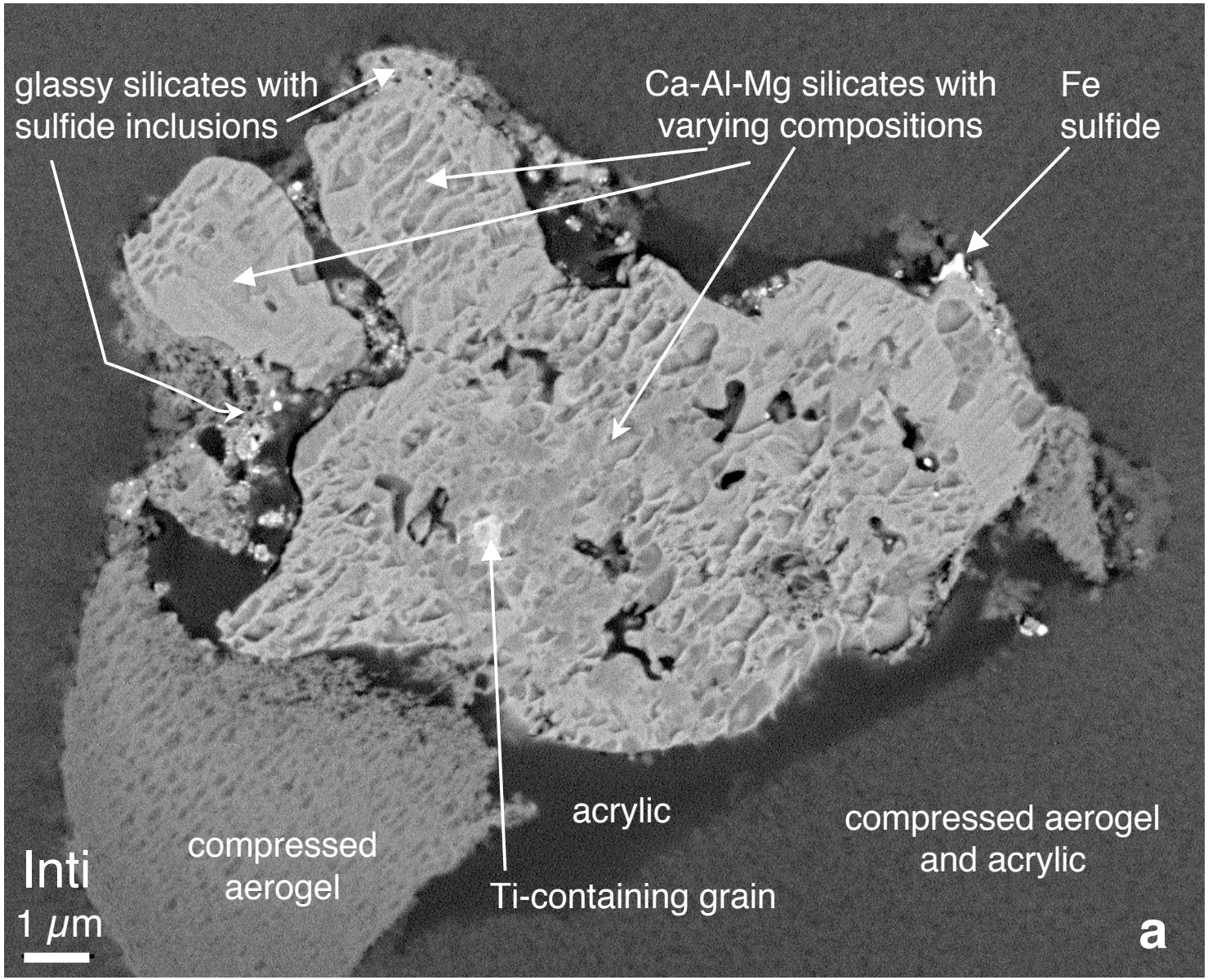
glassy silicates with
sulfide inclusions
Ca-Al-Mg silicates with
varying compositions
Fe
sulfide
acrylic
compressed
aerogel
Ti-containing grain
compressed aerogel
and acrylic
Inti
1 μm
a

Fig. 2a

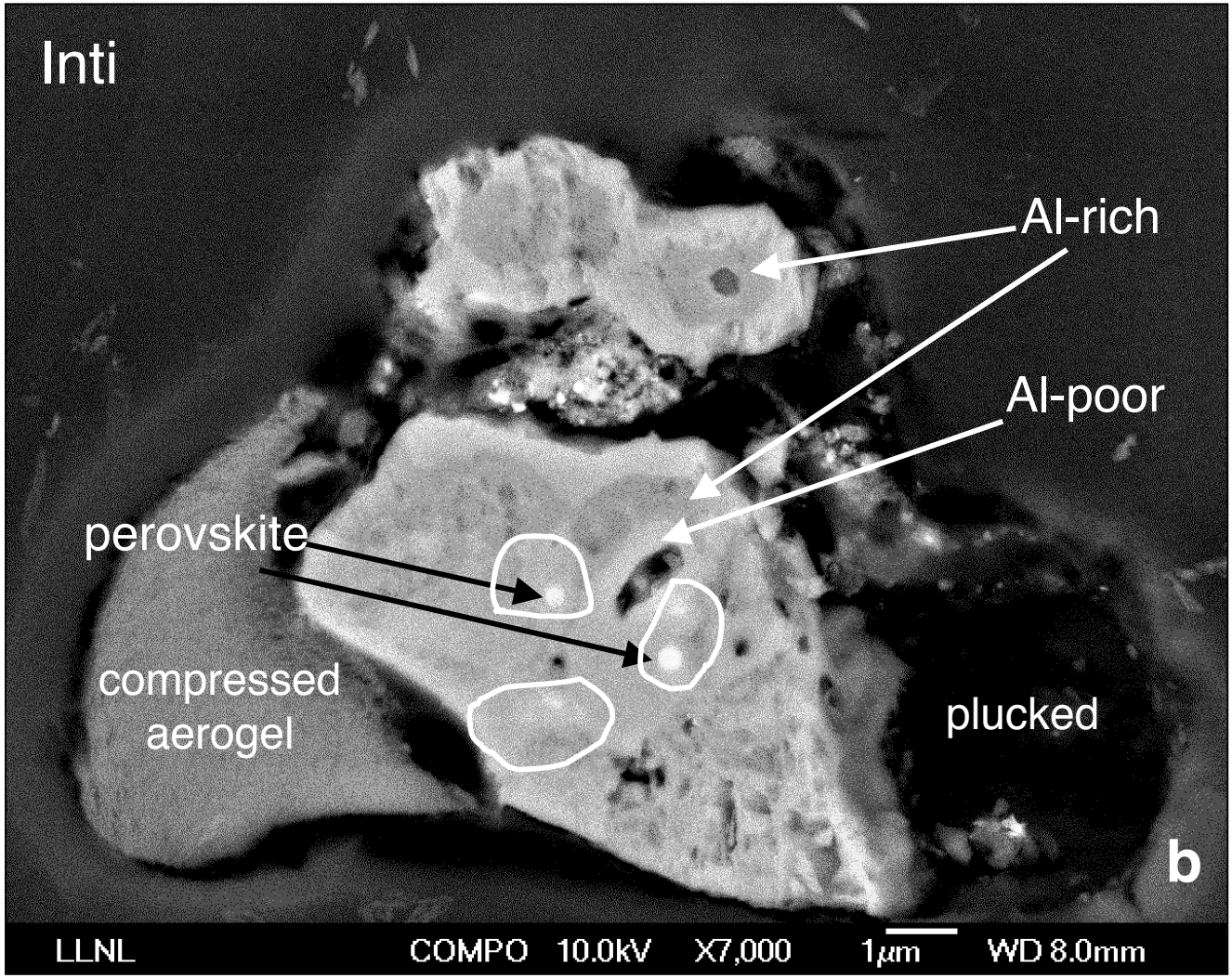
Inti
Al-rich
Al-poor
perovskite
compressed
aerogel
plucked
b
LLNL
COMPO 10.0kV X7,000 1μm WD 8.0mm

Fig. 2b

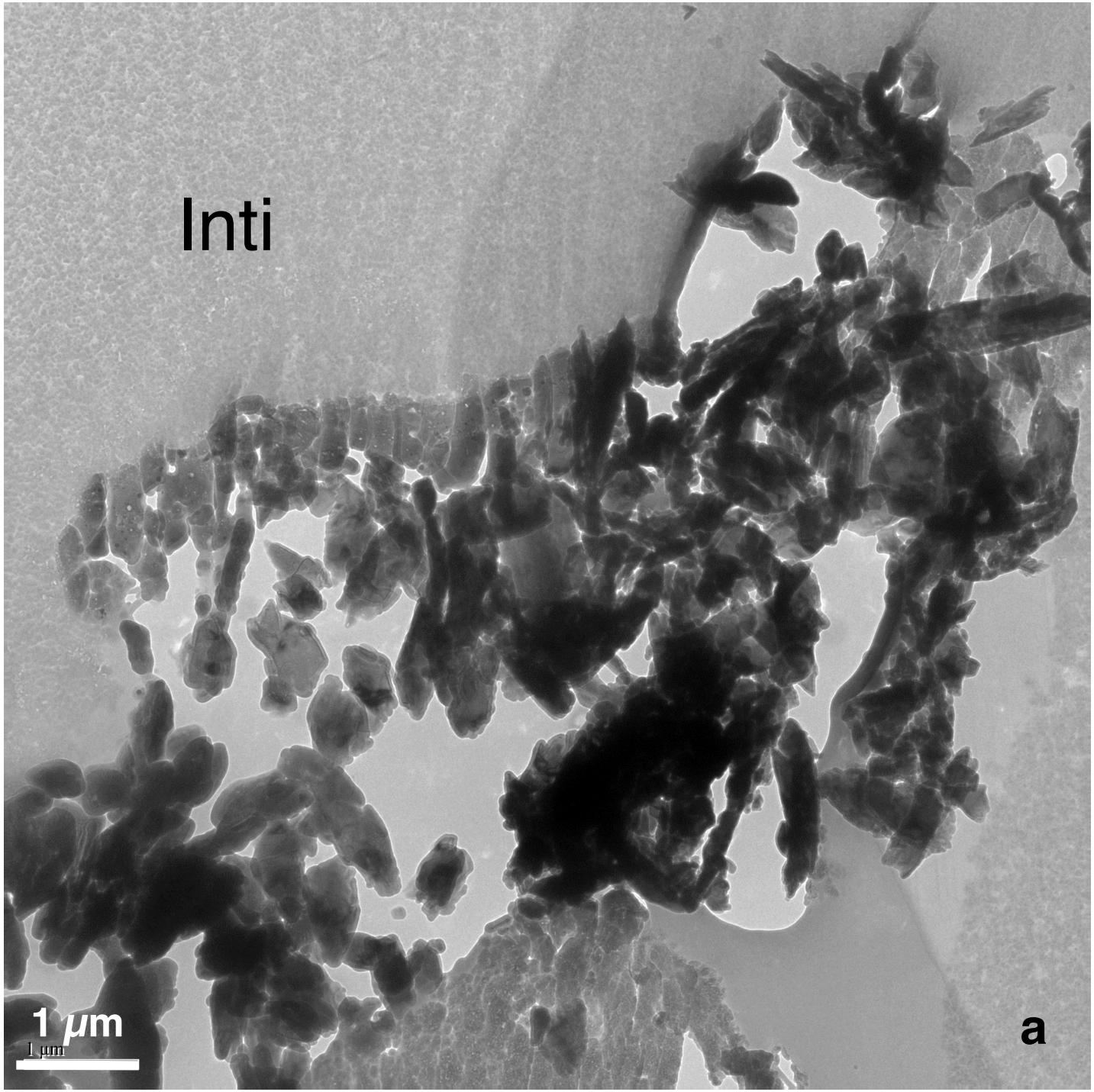

Fig. 3a

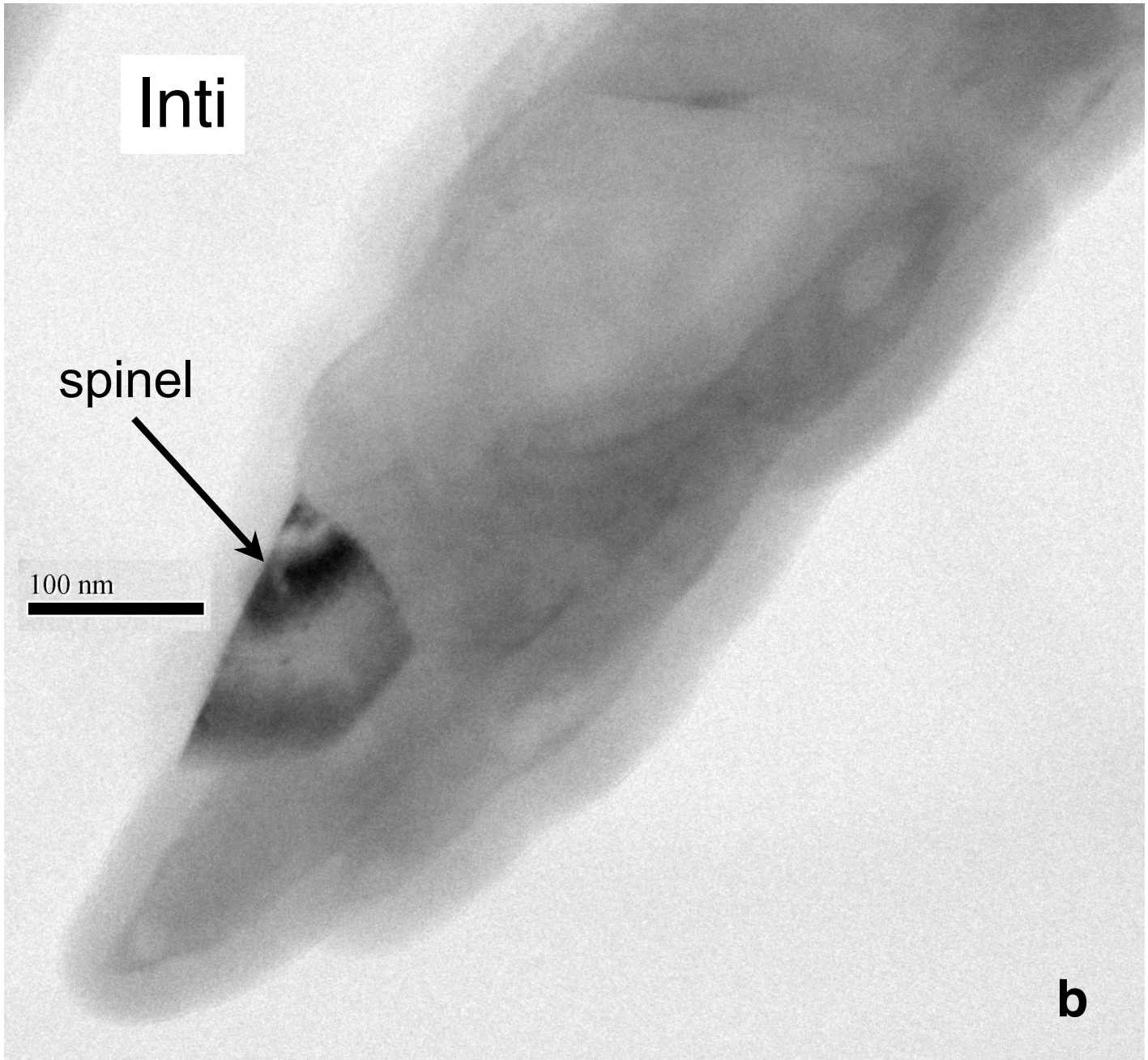

Fig. 3b

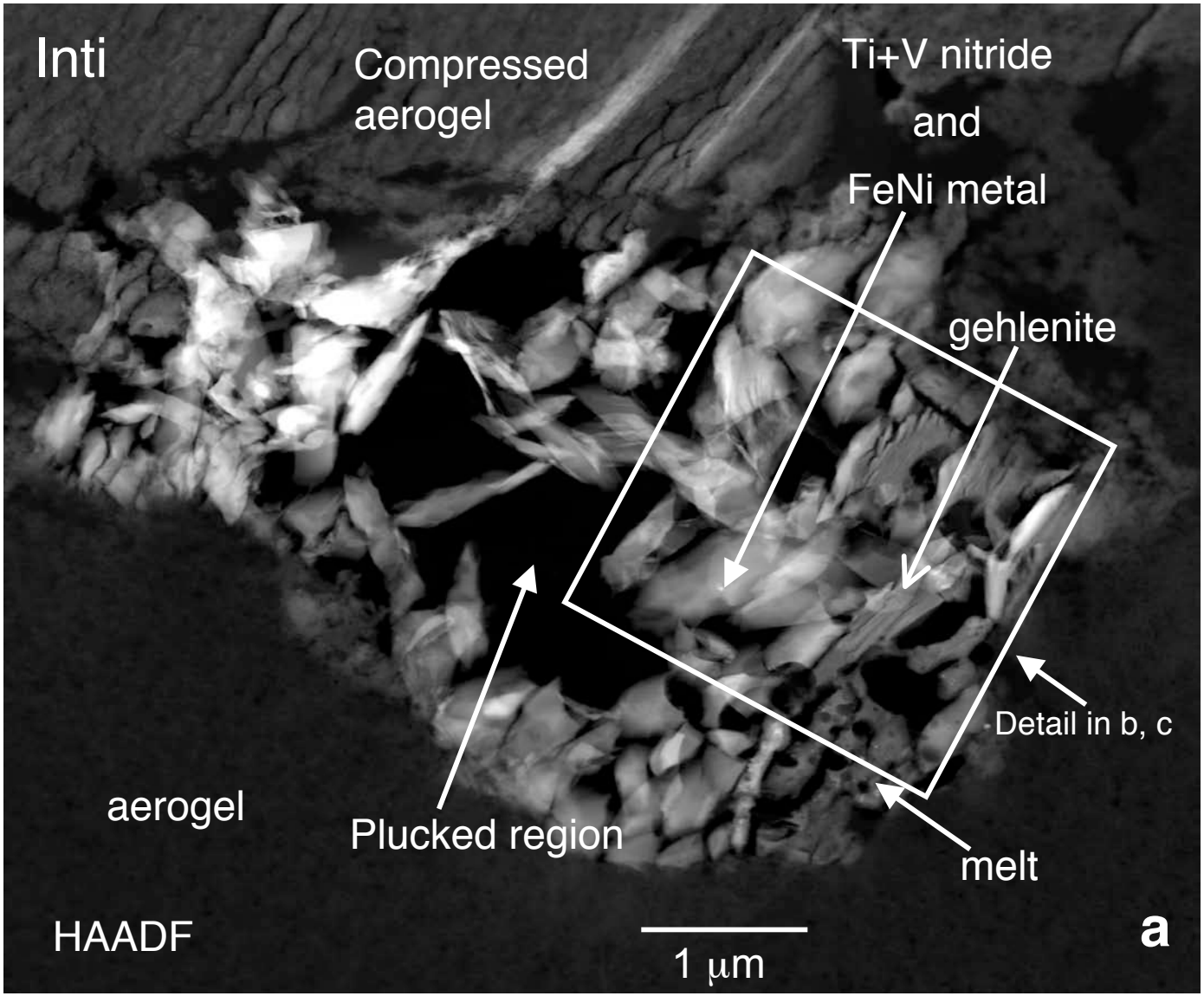
Inti
Compressed aerogel
Ti+V nitride and FeNi metal
gehlenite
Detail in b, c
aerogel
Plucked region
melt
HAADF
1 μm
a

Fig. 4a

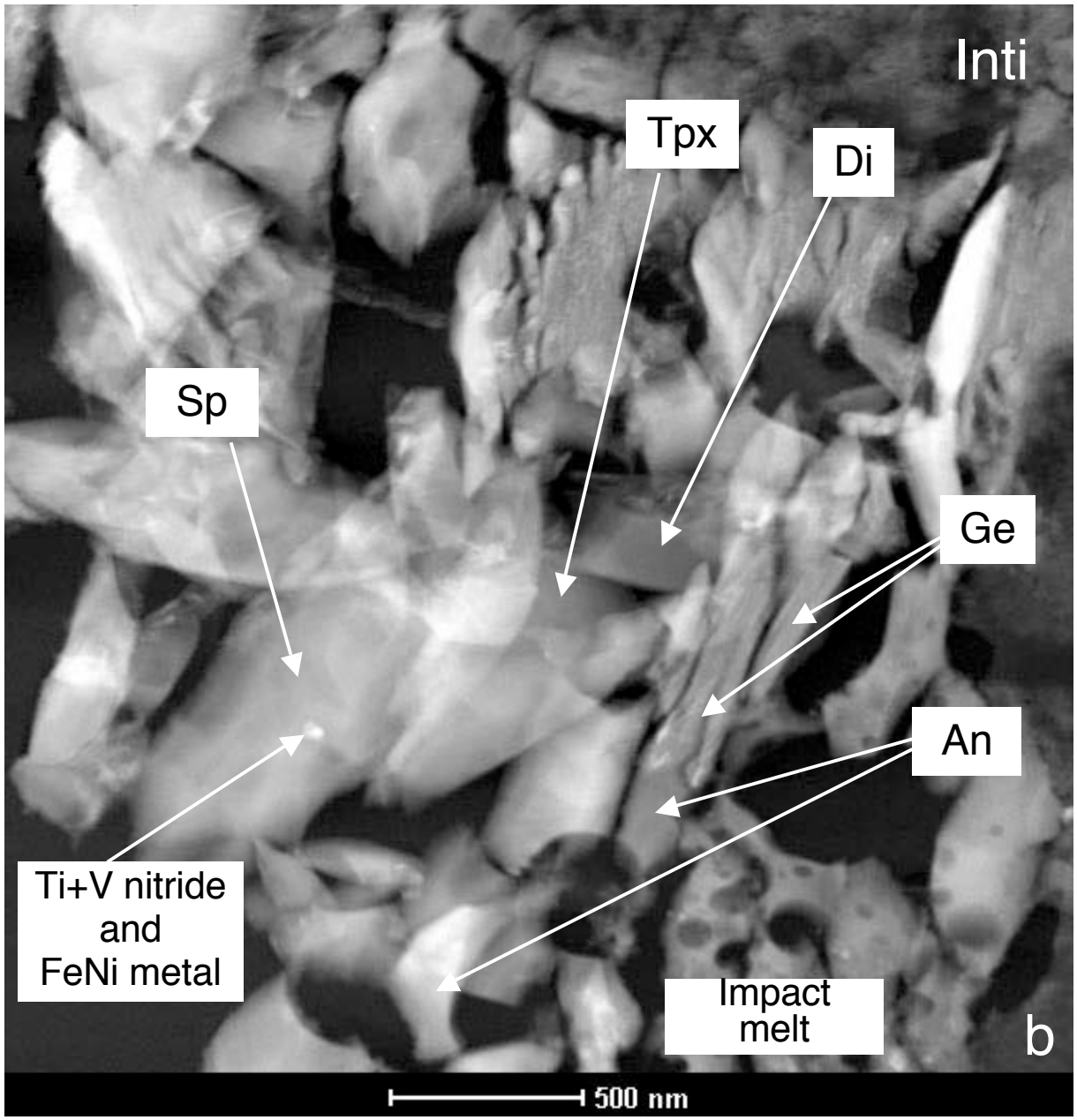
Inti
Tpx
Di
Sp
Ge
An
Ti+V nitride
and
FeNi metal
Impact
melt
b
500 nm

Fig. 4b

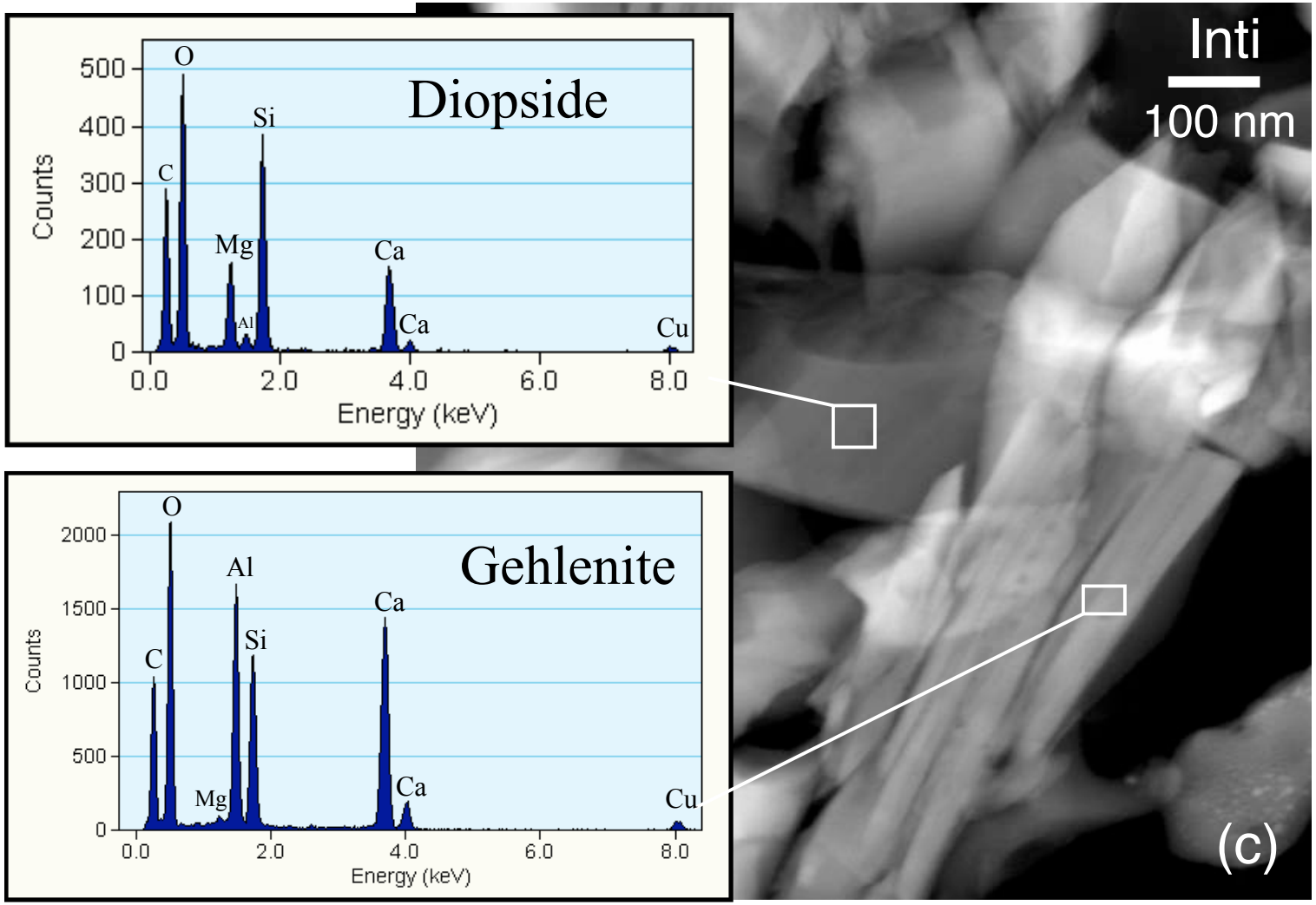
Diopside
Counts
Energy (keV)
O
C
Si
Mg
Al
Ca
Ca
Cu
0
100
200
300
400
500
0.0
2.0
4.0
6.0
8.0
Gehlenite
Counts
Energy (keV)
O
Al
C
Si
Ca
Mg
Ca
Cu
0
500
1000
1500
2000
0.0
2.0
4.0
6.0
8.0
Inti
100 nm
(c)

Fig. 4c

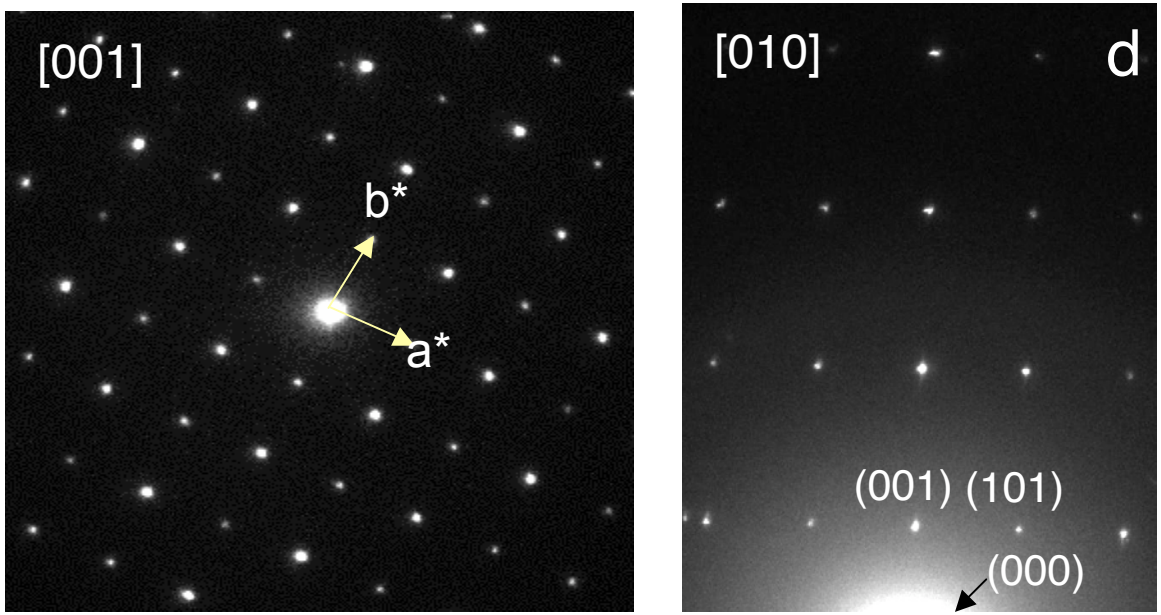

Fig. 4d

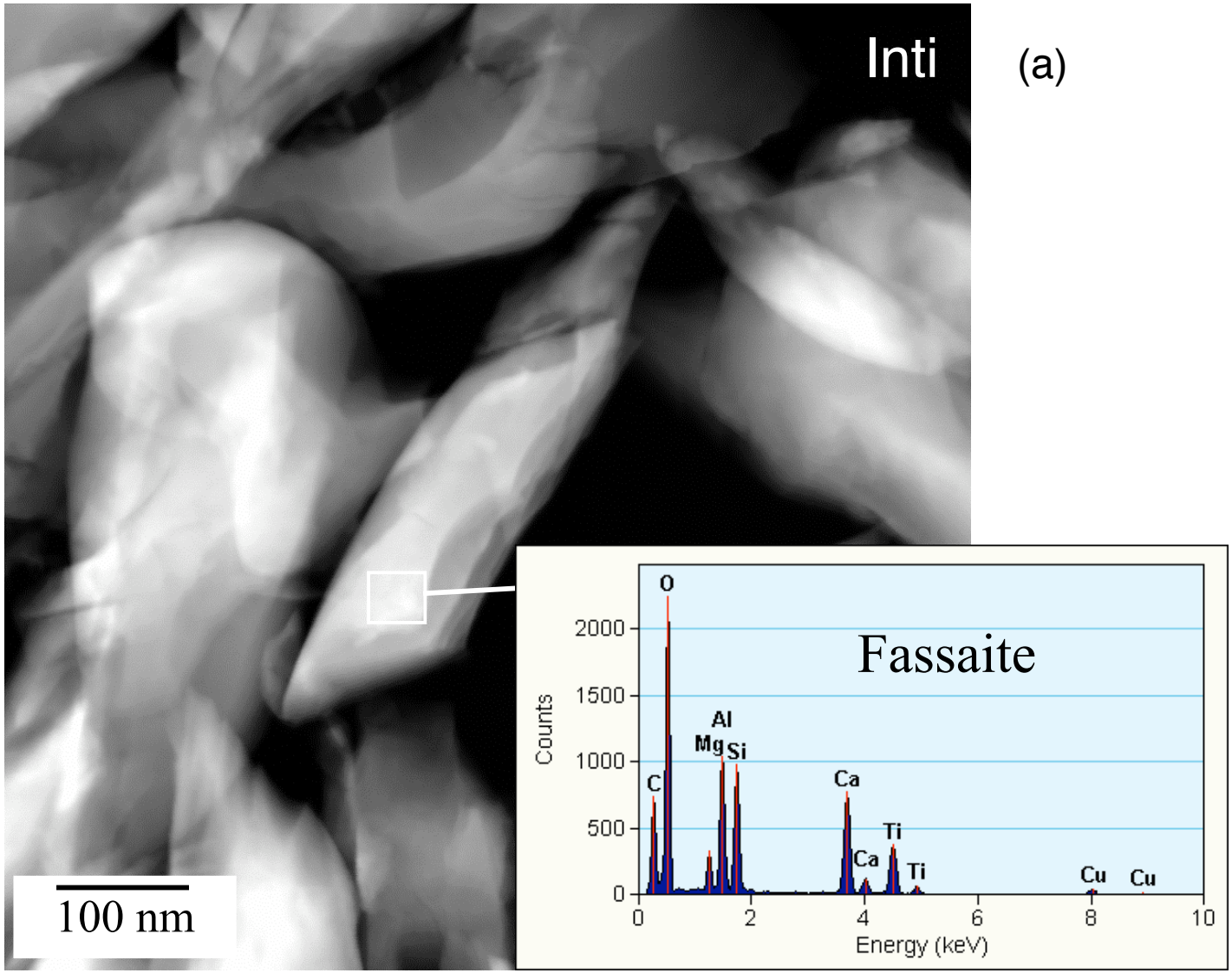
Inti
(a)
100 nm
Fassaite
Counts
Energy (keV)
O
C
Al
Mg
Si
Ca
Ca
Ti
Ti
Cu
Cu
0
500
1000
1500
2000
0
2
4
6
8
10

Fig. 5a

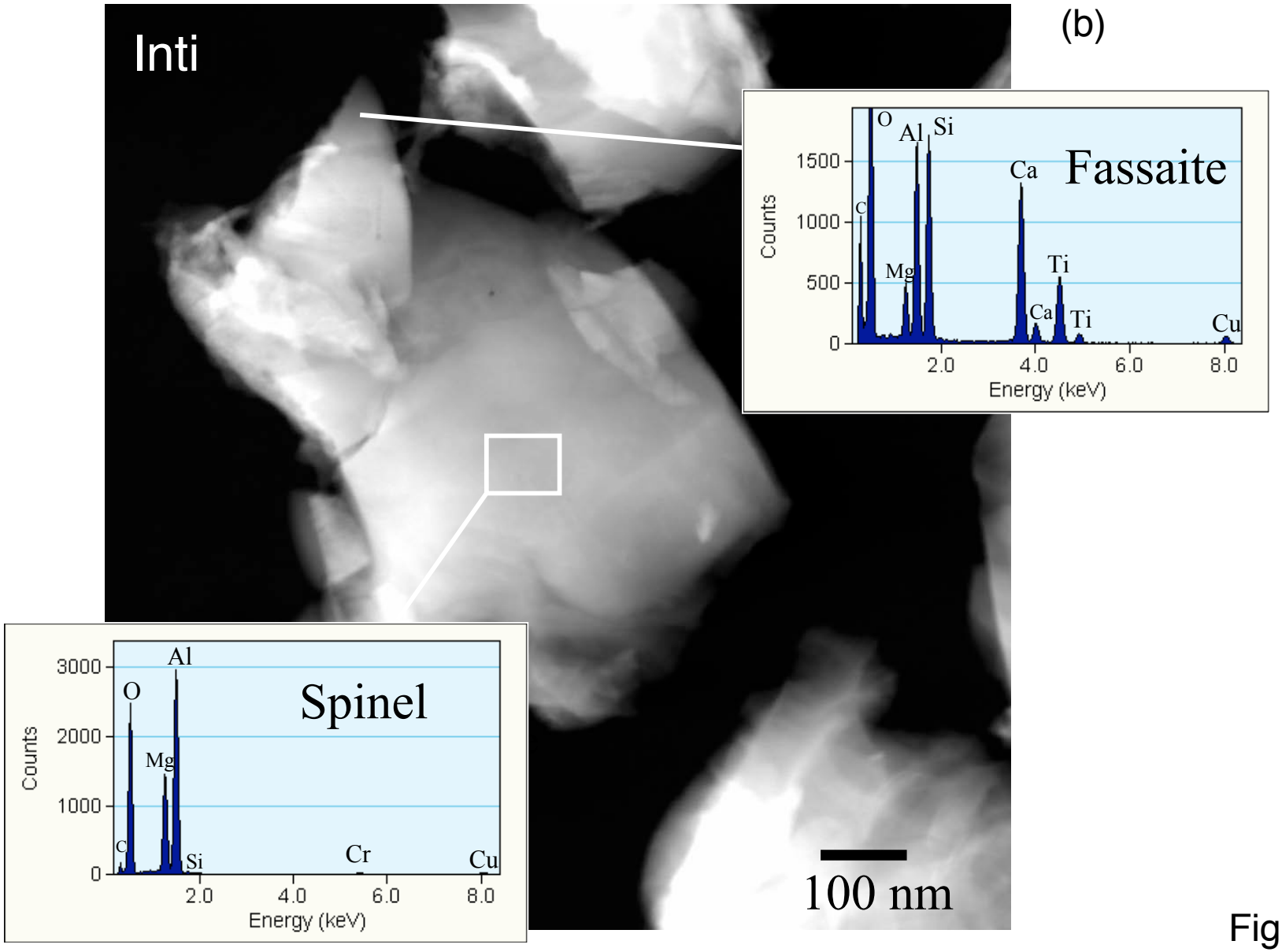
(b)
Inti
Fassaite
Counts
Energy (keV)
O
Al
Si
Ca
Mg
Ti
Cu
C
Spinel
Cr
100 nm

Fig. 5b

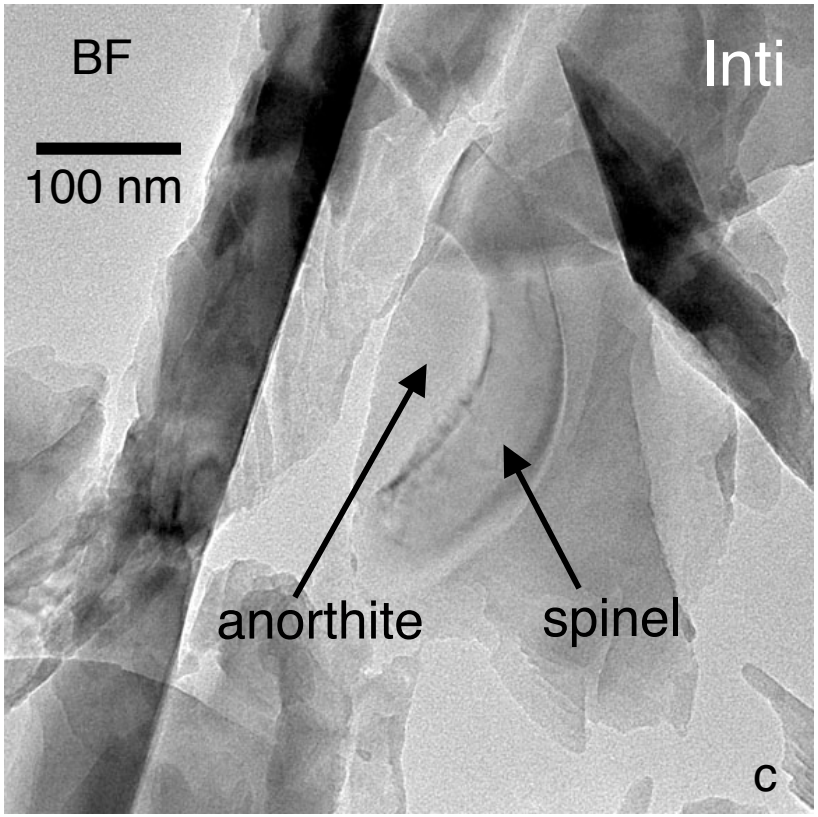

Fig. 5c

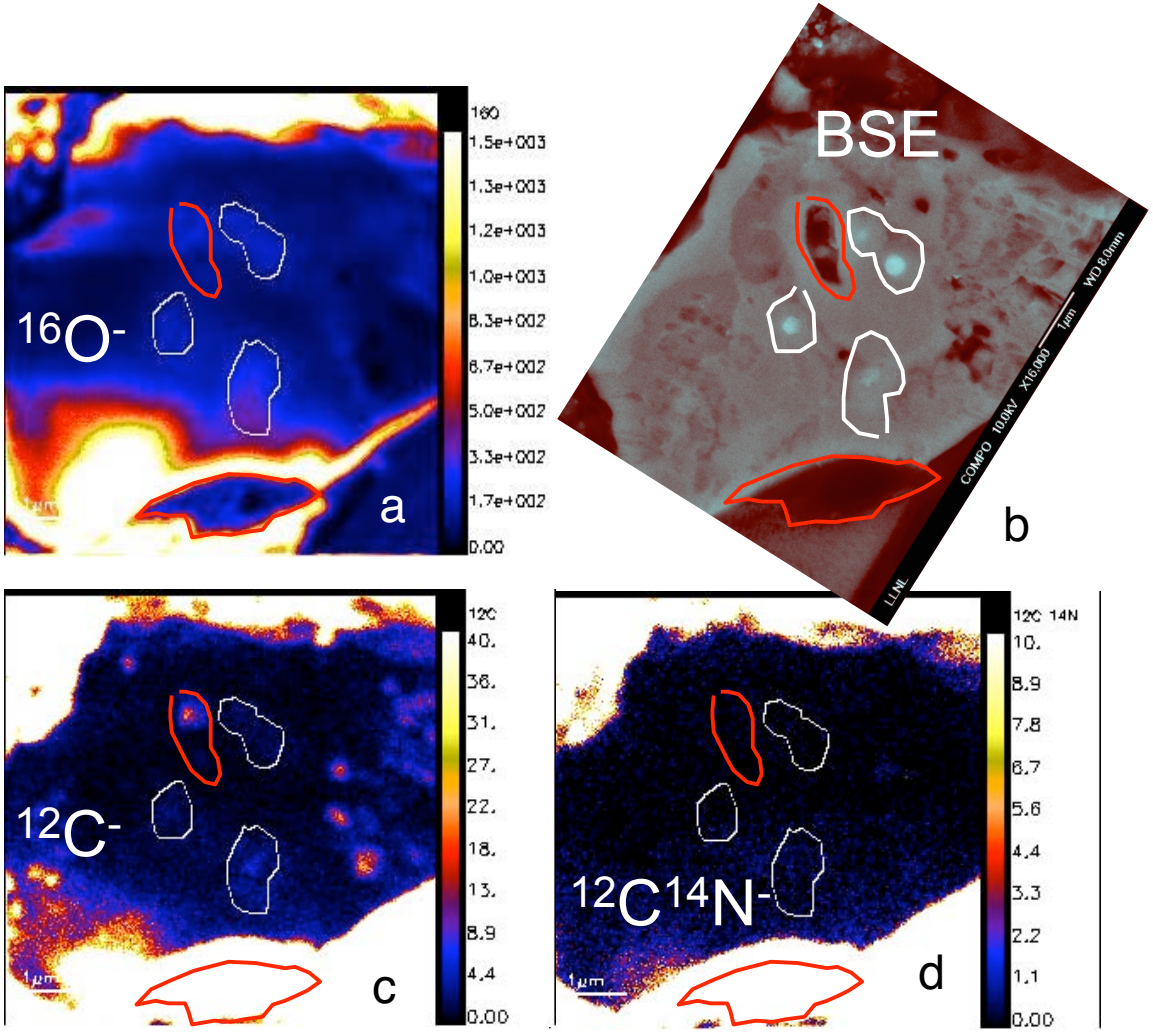
16O-
a
160
1.5e+003
1.3e+003
1.2e+003
1.0e+003
8.3e+002
6.7e+002
5.0e+002
3.3e+002
1.7e+002
0.00
BSE
b
12C-
c
12C
40.
36.
31.
27.
22.
18.
13.
8.9
4.4
0.00
12C14N-
d
12C 14N
10.
8.9
7.8
6.7
5.6
4.4
3.3
2.2
1.1
0.00

Fig. 6

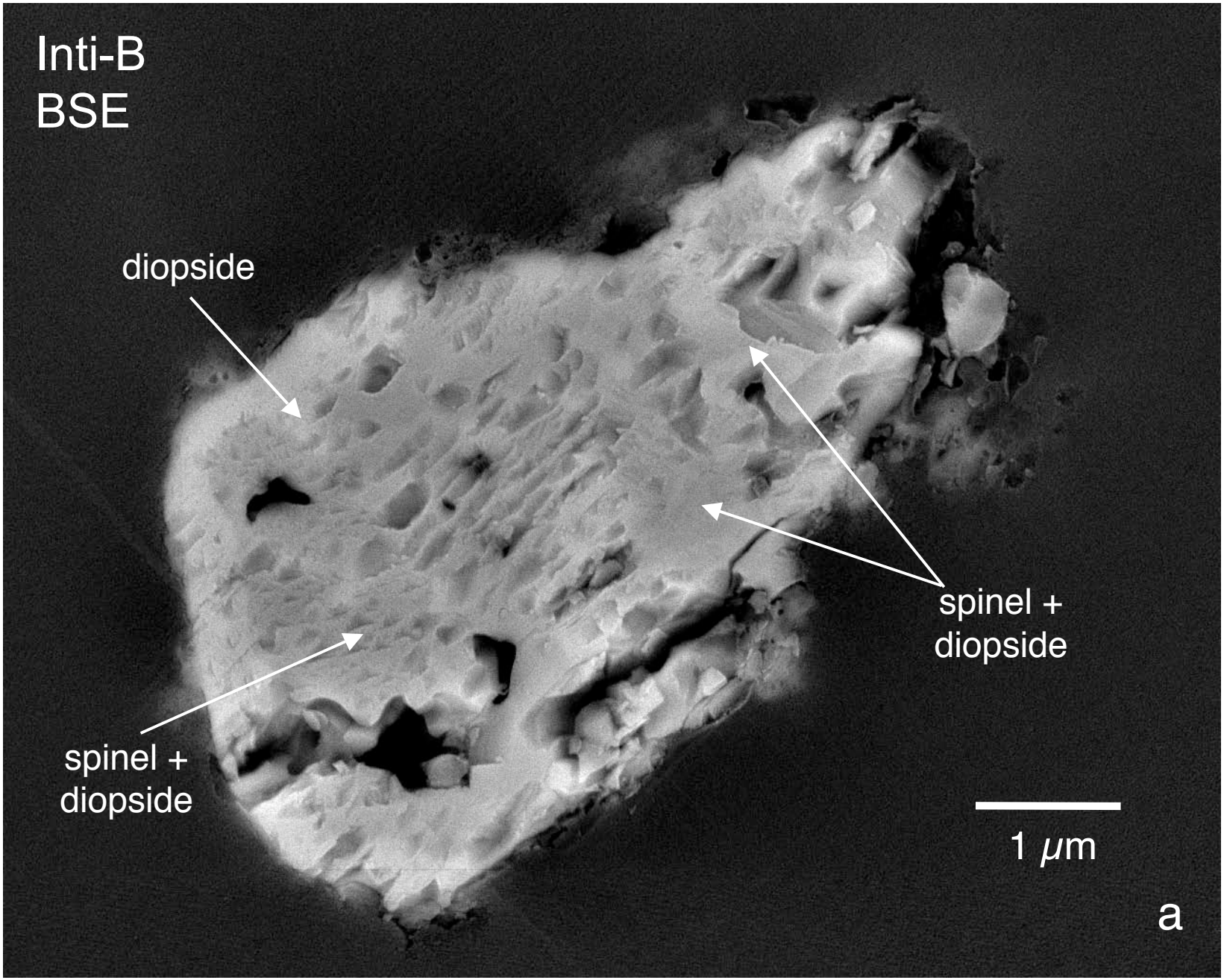

Fig. 7a

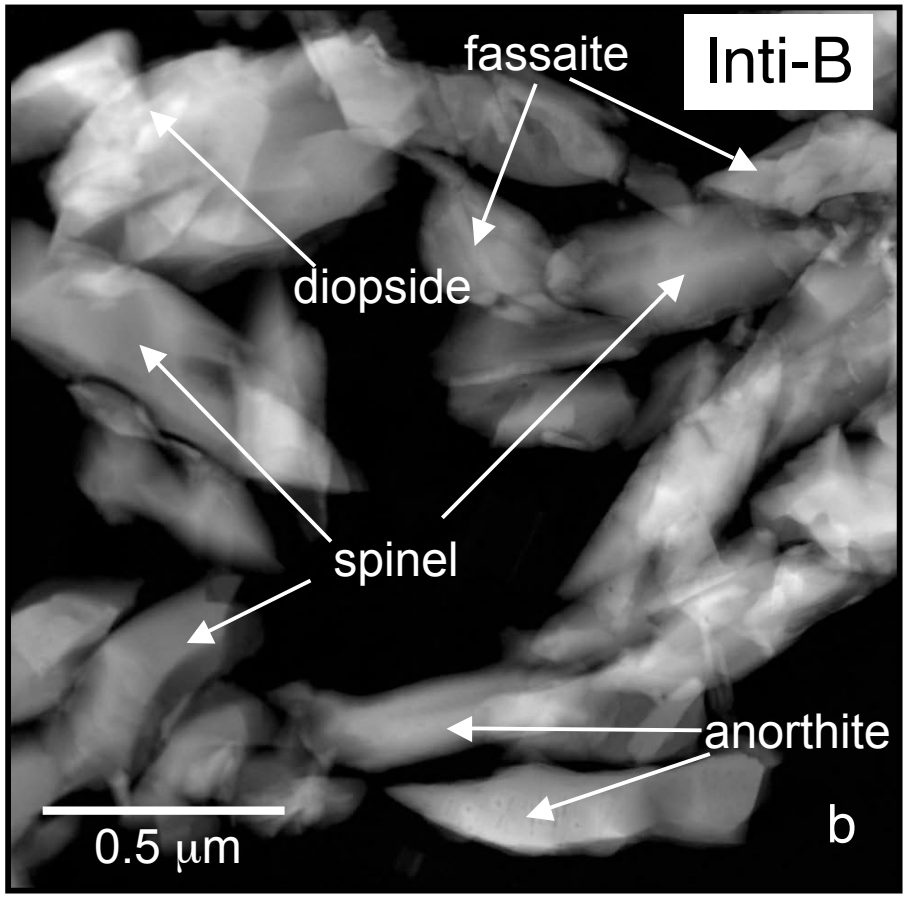

Fig. 7b

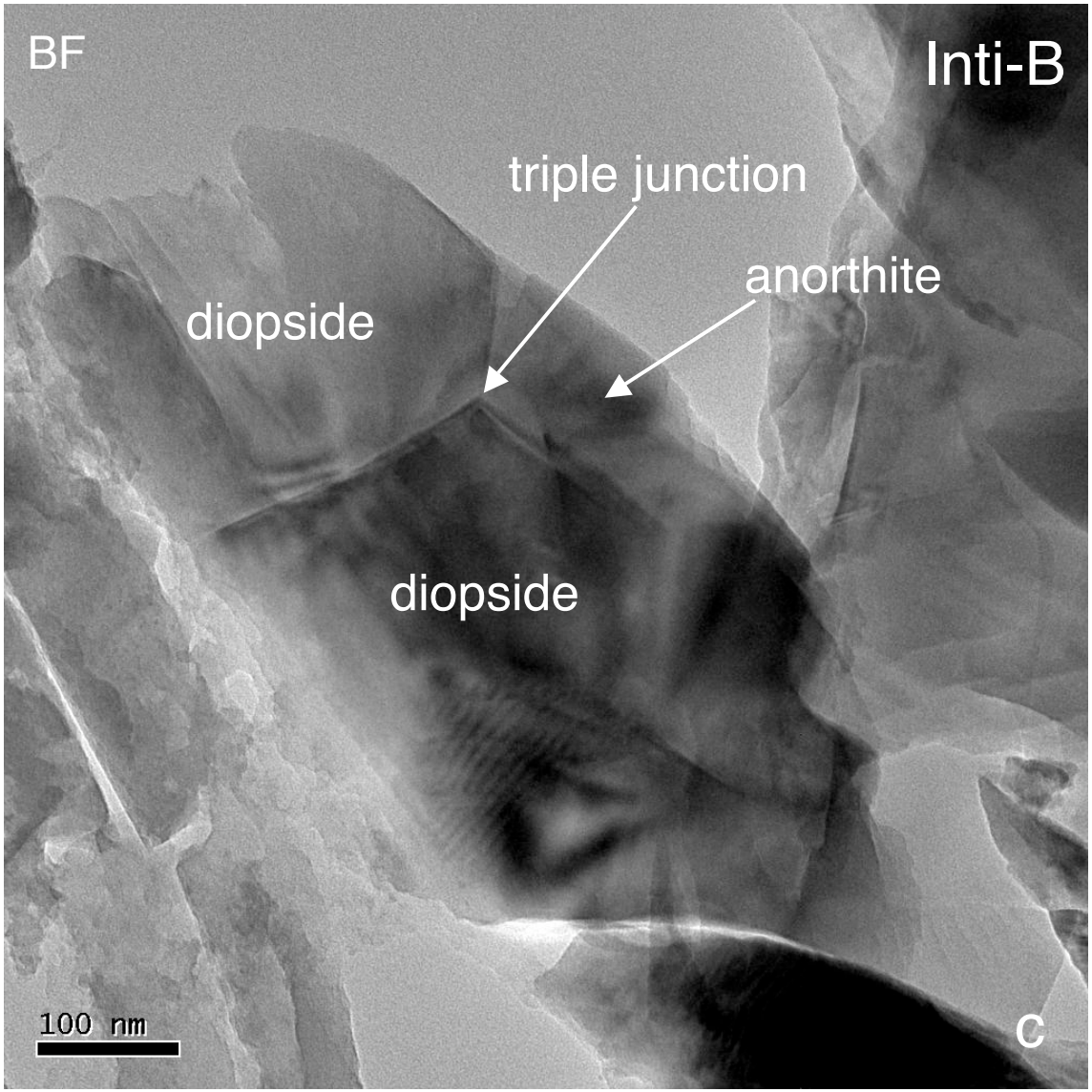
BF
Inti-B
triple junction
anorthite
diopside
diopside
100 nm
c

Fig. 7c

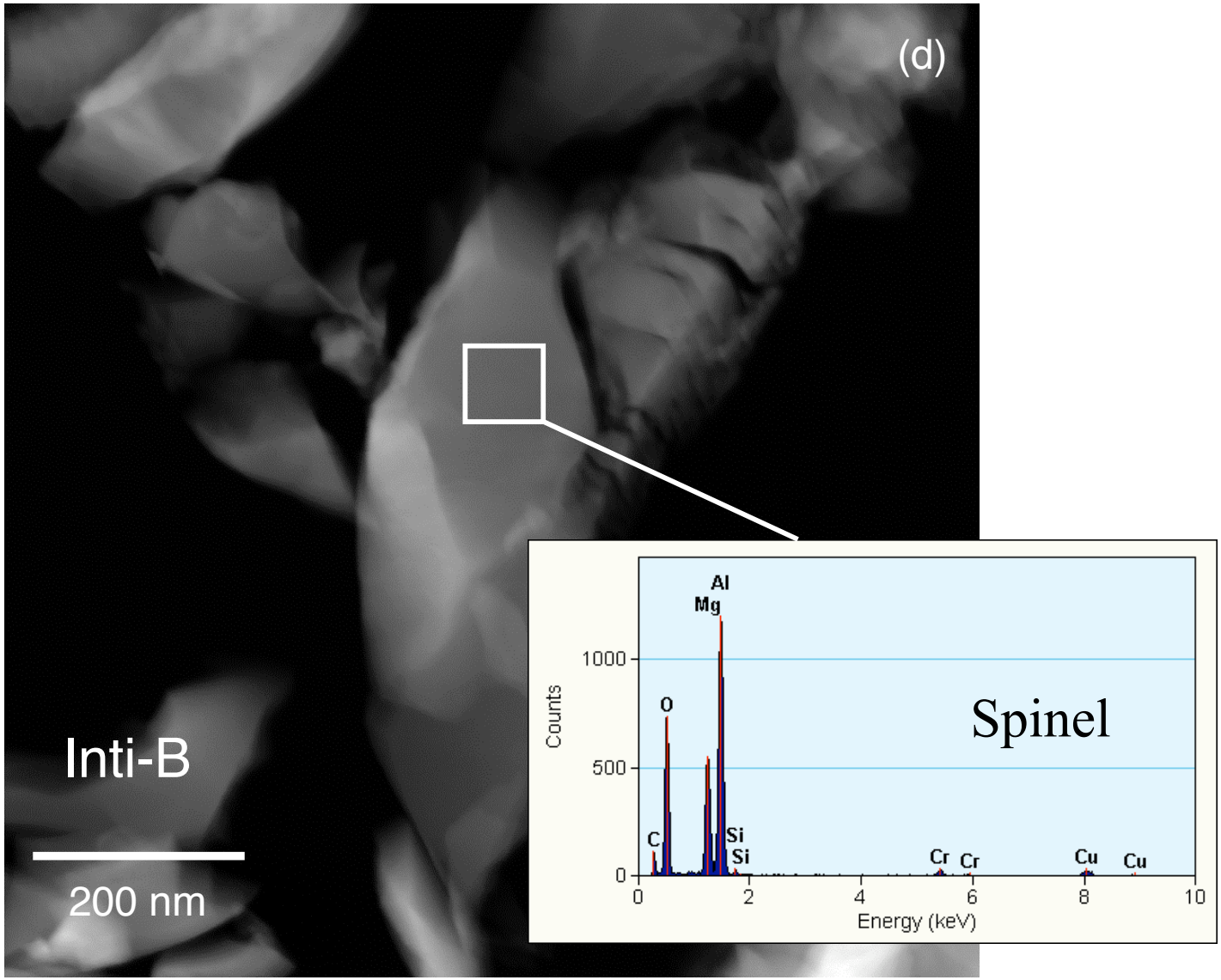
(d)
Inti-B
200 nm
Al
Mg
O
C
Si
Si
Cr
Cr
Cu
Cu
Spinel
Counts
1000
500
0
0
2
4
6
8
10
Energy (keV)

Fig. 7d

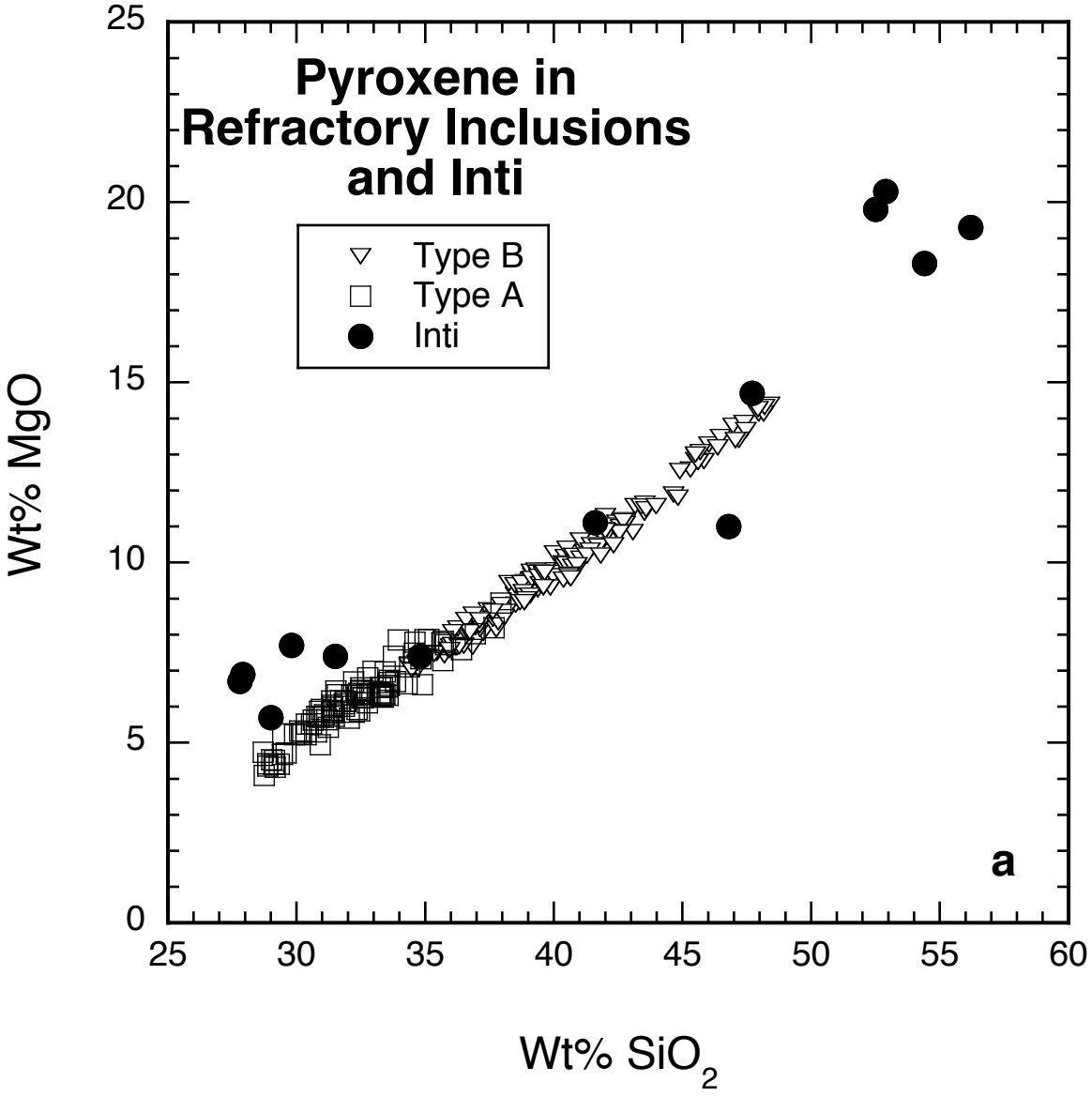
Pyroxene in
Refractory Inclusions
and Inti
Type B
Type A
Inti
a
Wt% MgO
Wt% SiO2
0
5
10
15
20
25
25
30
35
40
45
50
55
60

Fig. 8a

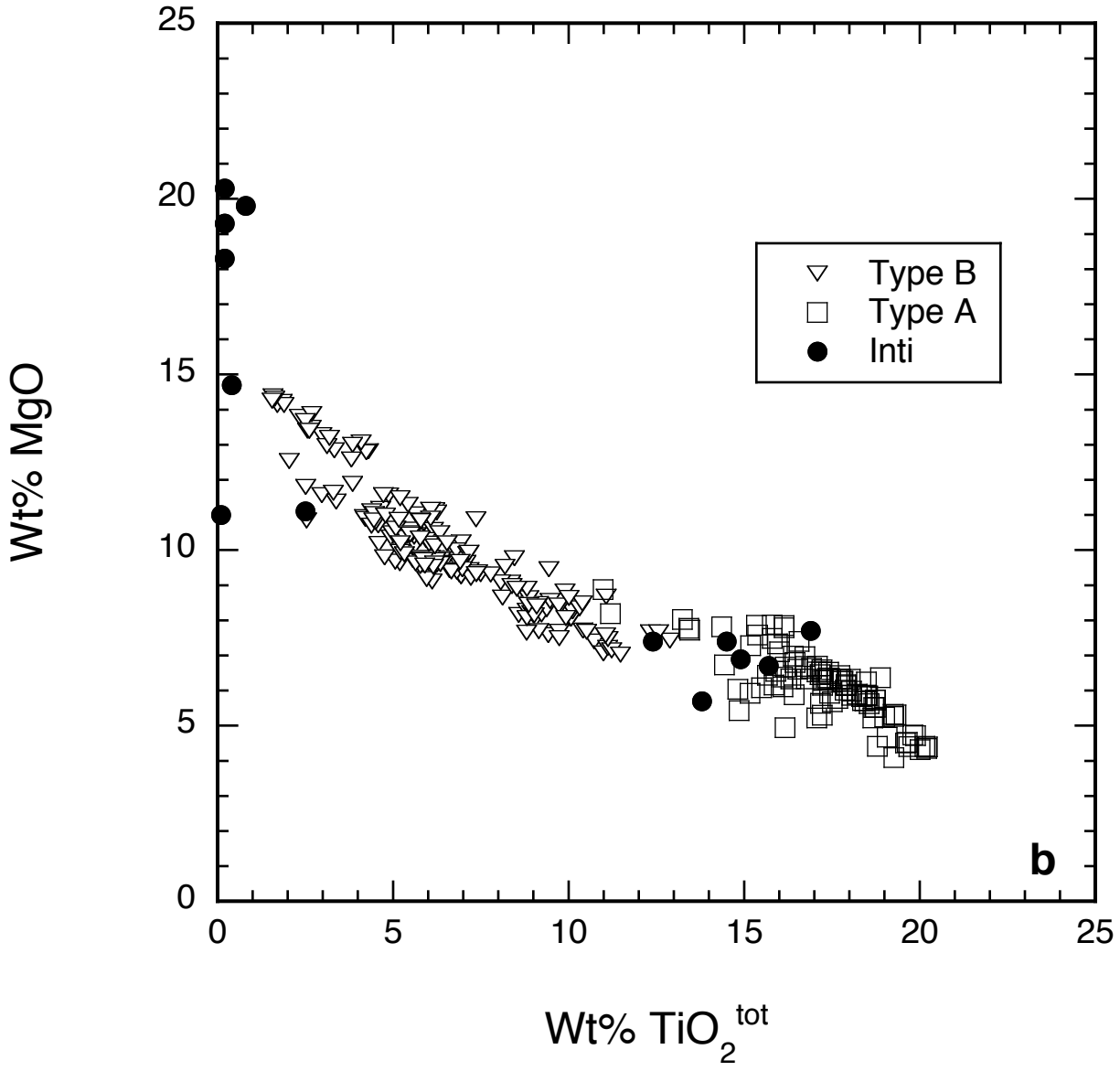

Fig. 8b

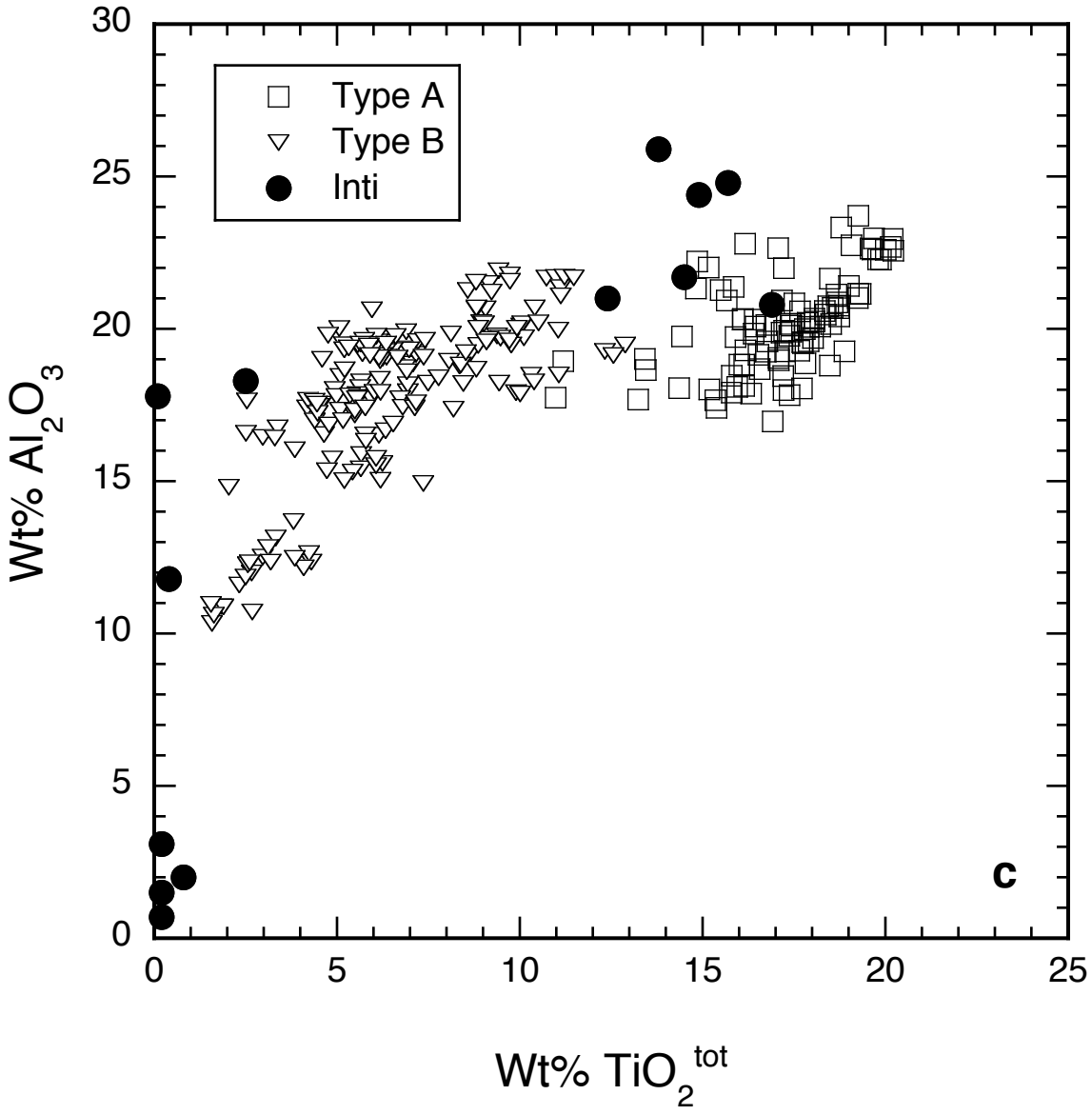

Fig. 8c

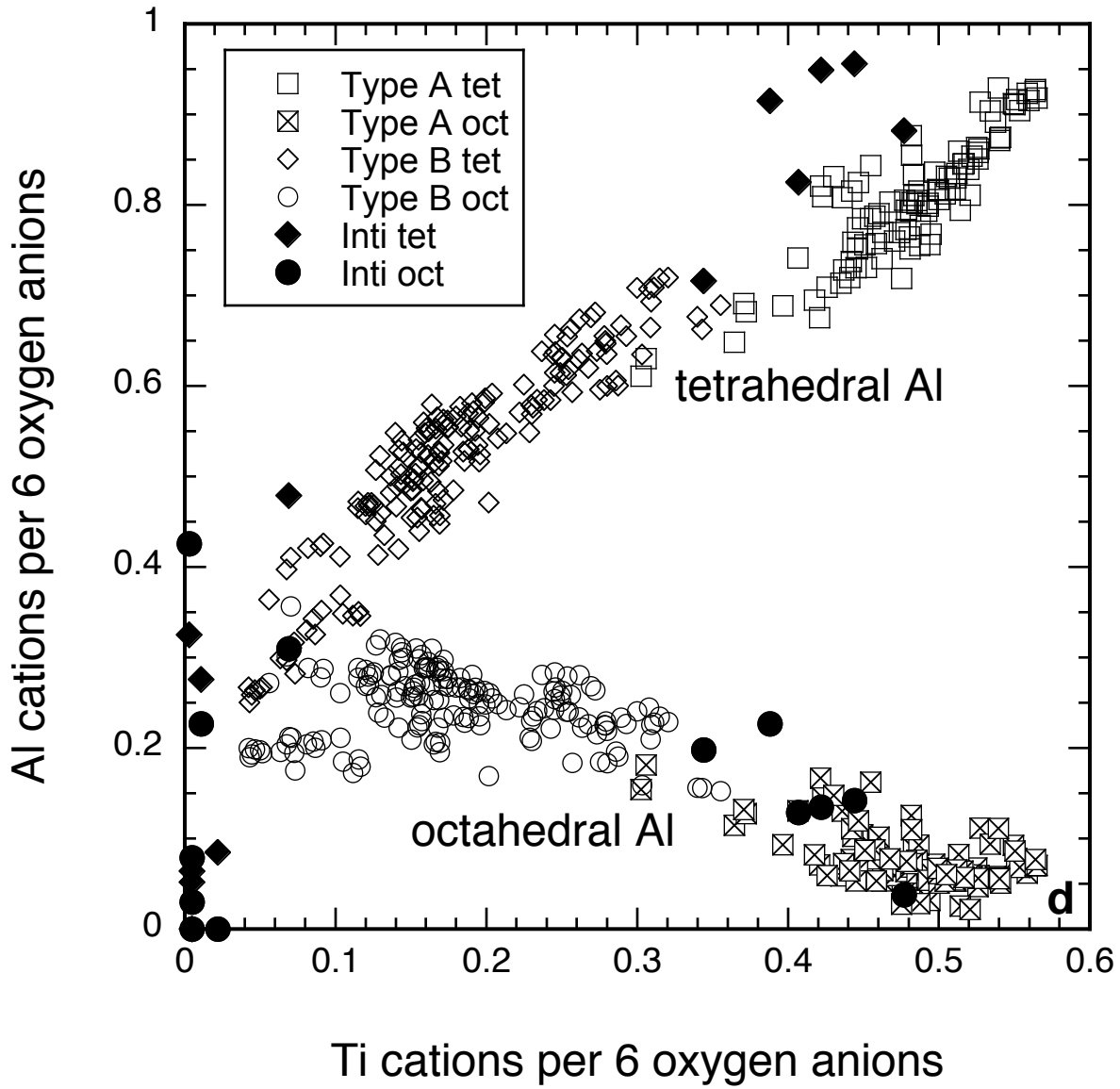
Type A tet
Type A oct
Type B tet
Type B oct
Inti tet
Inti oct
tetrahedral Al
octahedral Al
d
Al cations per 6 oxygen anions
Ti cations per 6 oxygen anions
0
0.2
0.4
0.6
0.8
1
0
0.1
0.2
0.3
0.4
0.5
0.6

Fig. 8d

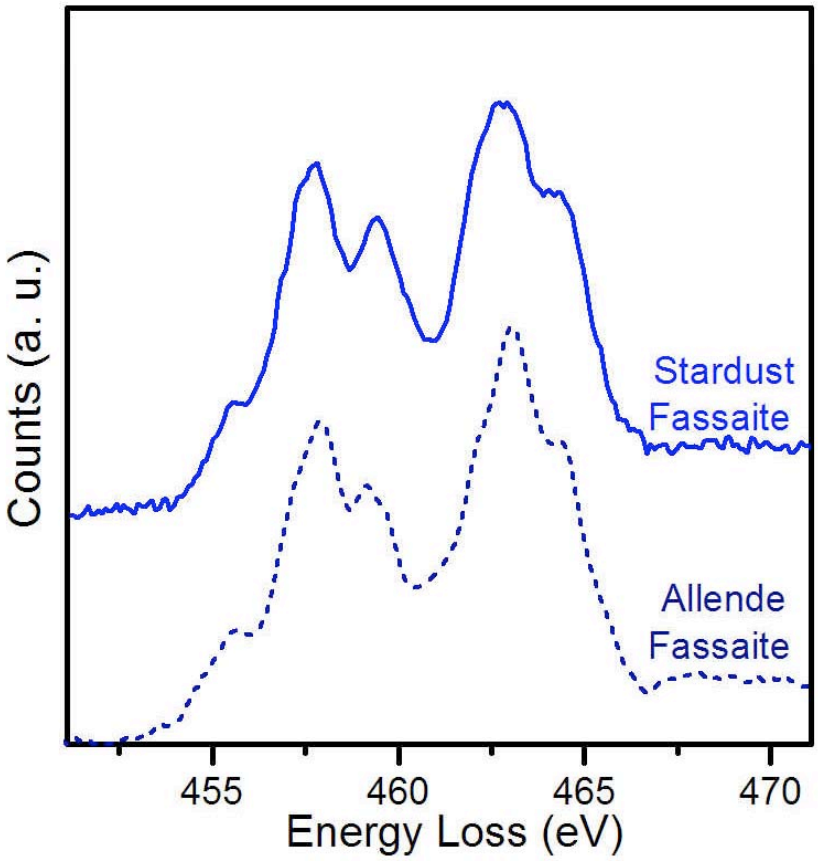
Counts (a. u.)
Stardust
Fassaite
Allende
Fassaite
455
460
465
470
Energy Loss (eV)

Fig. 9

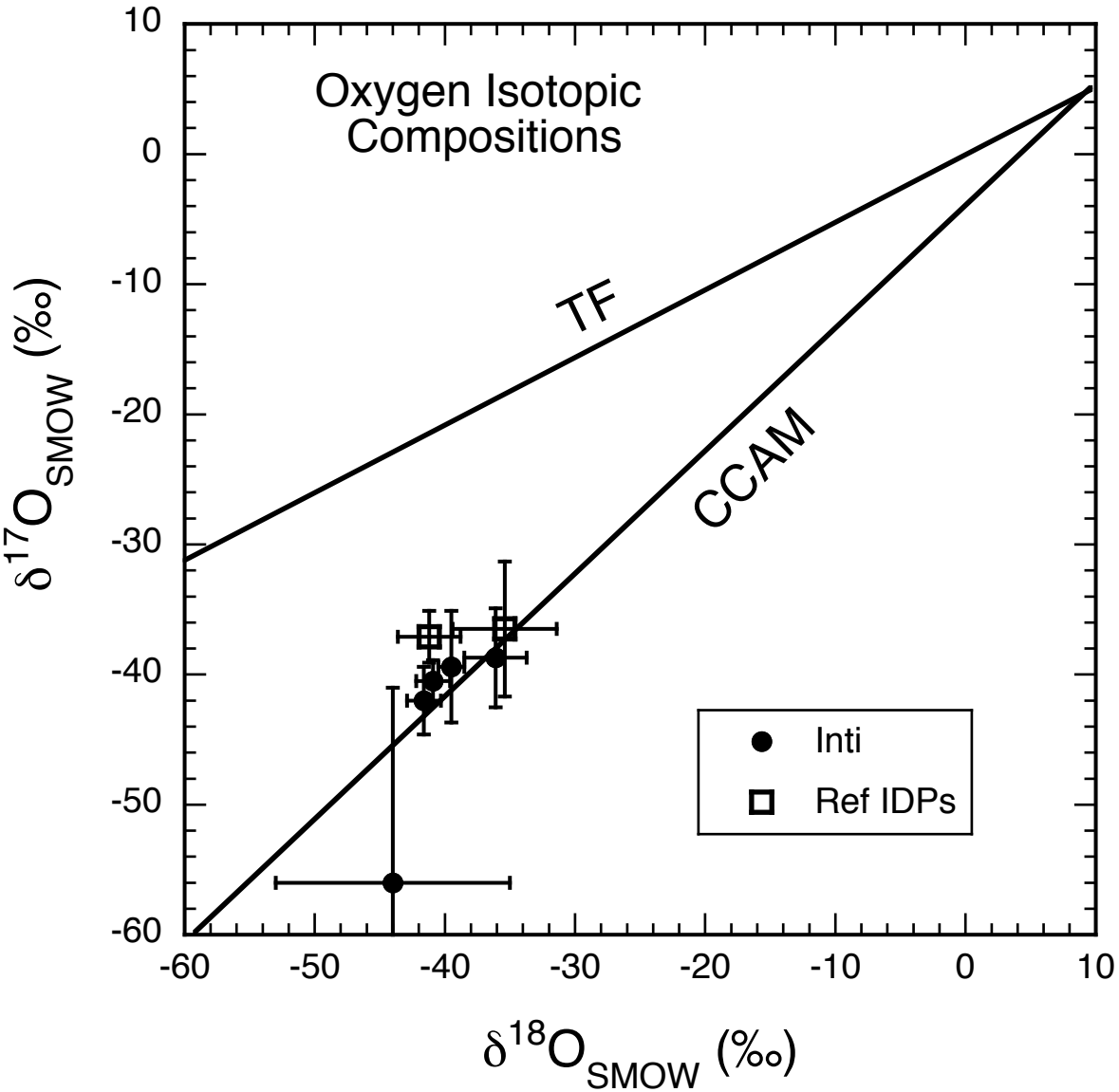
Oxygen Isotopic
Compositions
TF
CCAM
Inti
Ref IDPs
10
0
-10
-20
-30
-40
-50
-60
-60
-50
-40
-30
-20
-10
0
10
δ17OSMOW (‰)
δ18OSMOW (‰)

Fig. 10